iScience

CellPress

Article

Ras Post-transcriptionally Enhances a Pre-malignantly Primed EMT to Promote Invasion

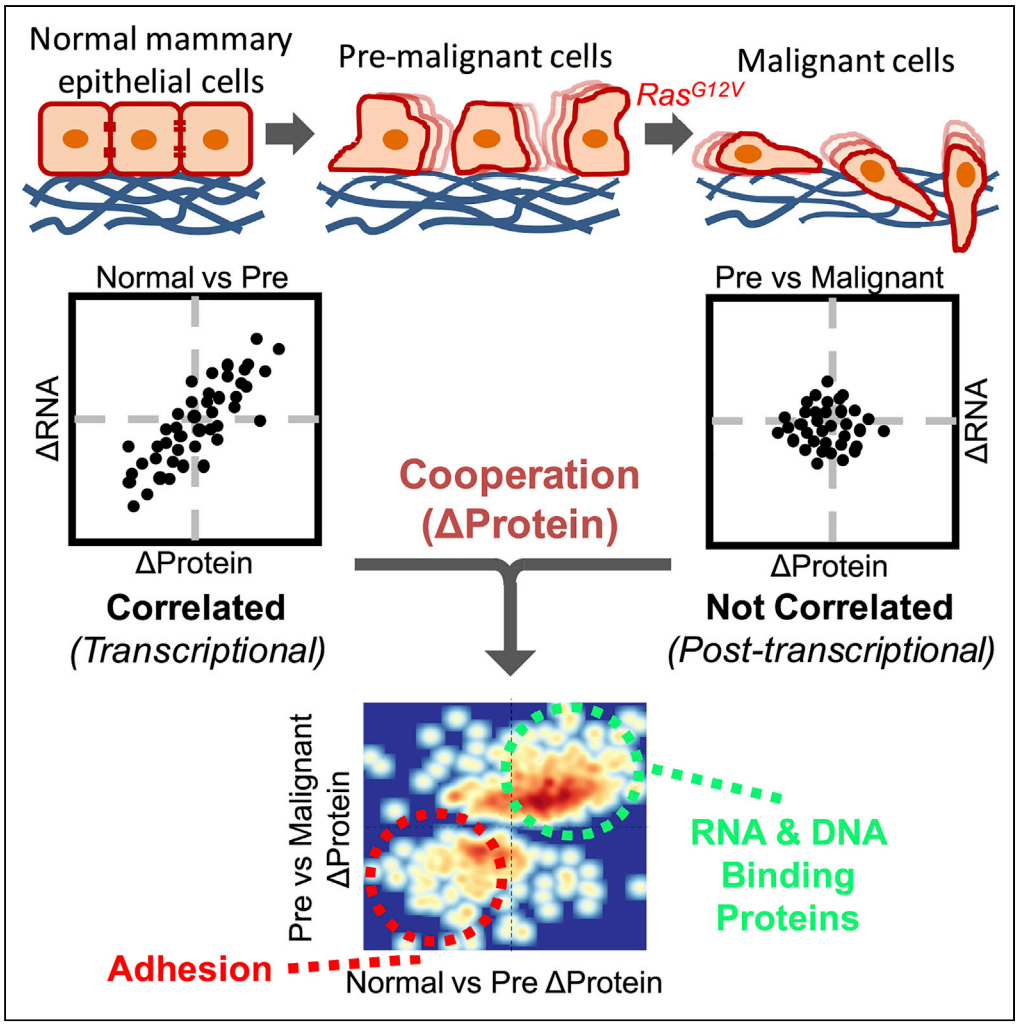

Laura S. Bisogno, Matthew B. Friedersdorf, Jack D. Keene

jack.keene@dm.duke.edu

HIGHLIGHTS

Two-stage progressive cell culture model demonstrates partial EMT states

Pre-malignant immortalization alters RNA abundance to induce cell migration

Ras transformation alters protein abundance, but not RNA, to induce cell invasion

Both stages cooperate to regulate protein expression of adhesion molecules and RBPs

Bisogno et al., iScience 4, 97–108
June 29, 2018
https://doi.org/10.1016/j.isci.2018.05.011

iScience

CellPress

Article

Ras Post-transcriptionally Enhances a Pre-malignantly Primed EMT to Promote Invasion

Laura S. Bisogno,[1,2] Matthew B. Friedersdorf,[1,2] and Jack D. Keene[1,3,*]

SUMMARY

Epithelial-to-mesenchymal transition (EMT) is integral to cancer progression, with considerable evidence that EMT has multiple intermediary stages. Understanding the mechanisms of this stepwise activation is of great interest. We recreated a genetically defined model in which primary cells were immortalized, resulting in migratory capacity, and subsequently H-Ras-transformed, causing malignancy and invasion. To determine the mechanisms coordinating stepwise malignancy, we quantified the changes in messenger RNA (mRNA) and protein abundance. During immortalization, we found dramatic changes in mRNA, consistent with EMT, which correlated with protein abundance. Many of these same proteins also changed following Ras transformation, suggesting that pre-malignant cells were primed for malignant conversion. Unexpectedly, changes in protein abundance did not correlate with changes in mRNA following transformation. Importantly, proteins involved in cellular adhesion and cytoskeletal structure decreased during immortalization and decreased further following Ras transformation, whereas their encoding mRNAs only changed during the immortalization step. Thus, Ras induced EMT-associated invasion via post-transcriptional mechanisms in primed pre-malignant cells.

INTRODUCTION

The epithelial-to-mesenchymal transition (EMT), a process by which epithelial cells lose epithelial properties and gain mesenchymal characteristics, is centrally involved in metastasis (Lambert et al., 2017; Nieto et al., 2016; Shibue and Weinberg, 2017). This program involves reorganization of the cytoskeleton, loss of junctions and apical-basal polarity, and activation of signaling mechanisms that promote motility and invasion as well as interactions between the tumor cell and the surrounding microenvironment, all of which can promote metastatic dissemination. There is much evidence that EMT is not a binary process, but rather a dynamic program with multiple intermediary stages of partial, or incomplete, EMT wherein cells have a mixture of both epithelial and mesenchymal characteristics (Nieto et al., 2016). In fact, the EMT program is usually only activated partially in human carcinomas, and partial EMT cells are observed in circulating tumor cells from patients with breast cancer (Yu et al., 2013). Underlying these transitions are changes in gene expression, including a set of prevalent transcriptional and alternative splicing changes (Lamouille et al., 2014; Shapiro et al., 2011; Warzecha et al., 2010; Yang et al., 2016). However, it is unclear how, and by what mechanisms, cancer-associated genetic mutations cooperate to promote transitions through EMT states.

Cancers are derived from normal cells that evolve stepwise and progressively to a neoplastic state (Hanahan and Weinberg, 2011). Although historically treated as a late-stage event, several studies have demonstrated that the acquisition of EMT-associated traits can occur early on during multi-step tumorigenesis (Husemann et al., 2008; Mani et al., 2008; Podsypanina et al., 2008; Rhim et al., 2012). Cell culture models typically utilize cell lines that are already immortalized, and thus abnormal. Therefore, a more informative cell culture model with which to study the mechanisms regulating the earliest stages of tumorigenesis and EMT would be one that starts with normal human epithelial cells and perturbs only the pathways required for cell immortalization and subsequent tumorigenesis. Pioneering work in the Weinberg laboratory demonstrated that normal human epithelial and fibroblast cells can be converted to a tumorigenic state by expressing viral proteins SV40 T-Ag and t-Ag and mammalian proteins hTERT and $HRas^{G12V}$(Hahn et al., 1999). Later work expanded these findings and identified a core set of non-viral proteins that together drive the processes of immortalization and transformation (Kendall et al., 2005, 2006). With the modified system, the introduction of hTERT, $p53^{DD}$, cyclin D1, $CDK4^{R24C}$, and $c\text{-}MYC^{T58A}$ to primary epithelial cells immortalizes the cells, whereas subsequent expression of $HRAS^{G12V}$ converts the immortalized cells to a

[1]Department of Molecular Genetics & Microbiology, Duke University Medical Center, Durham, NC 27710, USA

[2]These authors contributed equally

[3]Lead Contact

*Correspondence: jack.keene@dm.duke.edu

https://doi.org/10.1016/j.isci.2018.05.011

fully tumorigenic state. Using this approach, well-defined genetic models of tumorigenesis can be established starting with normal primary epithelial cells. It was previously demonstrated that the Ras-transformed human mammary epithelial cells (HMECs), but not the pre-malignant immortalized line, form tumors in immunocompromised mice. The resulting tumors were surrounded by areas marked by local tissue invasion (Kendall et al., 2005), a characteristic associated with EMT.

We reconstructed this genetically defined cell culture system of stepwise tumorigenesis as a model with which to study global regulation of early transitions to both malignancy and EMT at multiple levels of gene expression. We demonstrate here that pre-malignant, immortalized cells have gained migratory capacity, whereas the Ras-transformed cells are significantly more invasive, indicating a stepwise gain of traits typically associated with EMT and metastasis. To determine the mechanisms of malignant progression, we quantified changes in messenger RNA (mRNA) expression using RNA sequencing and protein expression using ultraperformance liquid chromatography-tandem mass spectrometry (UPLC-MS/MS). Following immortalization, we found dramatic changes in mRNA expression and processing, which correlated with protein abundance. These changes were consistent with previously reported EMT mRNA and alternative splicing signatures. Surprisingly, during Ras transformation we observed enhanced changes of many of the same EMT-related proteins that previously changed during primary cell immortalization, whereas there were very few changes that were unique to the transformation step. These findings suggest that the pre-malignant cells were primed for malignant conversion, with immortalization and transformation cooperating to promote changes in protein abundance. Unlike the immortalization step, changes in protein abundance did not correlate with changes in mRNA following transformation, suggesting significant involvement of post-transcriptional regulation, rather than being solely driven by transcription. Thus, although the two sequential stages appear to cooperate, they use distinct mechanisms to promote EMT. For example, proteins involved in cellular adhesion and cytoskeletal structure, such as α-adducin (ADD1), decreased during immortalization and decreased further following Ras transformation, but their encoding mRNAs did not decrease during Ras transformation. Moreover, short hairpin RNA (shRNA) knockdown of ADD1 in pre-malignant cells resulted in a striking increase in invasive capacity, similar to what we observed in the Ras-transformed cells. Taken together, our data reveal that both malignancy and EMT-associated migration and invasion can be initiated in a two-stage process involving transcriptome priming of pre-malignant cells followed by Ras-triggered post-transcriptional regulation.

RESULTS

Pre-malignant Immortalized Cells Have a Migratory Phenotype, whereas Ras-Transformed Cells Have Increased Invasive Capacity

To study cancer progression, we used a cell culture model in which we immortalized primary HMECs (PRIM) through the stable expression of hTERT, $p53^{DD}$, cyclinD1, $CDK4^{R24C}$, and $c\text{-}Myc^{T58A}$ transgenes. This pre-malignant, immortalized cell line (IMO) was used to create a third, Ras-transformed cell line (TFO) through the expression of $H\text{-}Ras^{G12V}$ (Figure 1A). We previously confirmed the expression of all transgenes in these cells with quantitative reverse-transcriptase polymerase chain reaction (qRT-PCR), demonstrated that only the TFO cells have anchorage-independent growth using a standard soft agar assay, and confirmed that IMO and TFO cells can be passaged indefinitely, in contrast to the PRIM cells (Bisogno and Keene, 2017). Interestingly, PRIM cells grew in distinct clusters, whereas IMO and TFO cells had a scattered pattern (Figure S1), suggesting altered cell adhesion properties.

To investigate the migratory properties of IMO and TFO cells, we measured wound closure using a scratch assay. Cells were grown to confluency, and a single scratch was made in the cell monolayer. Migration was quantified as the degree of wound closure after 24 hr, and both IMO and TFO cells were migratory with no significant difference in migration (Figure 1B). We quantified invasion of these cell lines using a Transwell Matrigel invasion assay, and, in contrast to migration, Ras transformation significantly increased invasiveness (Figure 1C). Given that migration and invasion are closely linked to EMT, these results suggest that this genetically defined, primary cell-derived system of tumorigenesis can serve as a stepwise model of gain for EMT-associated properties.

Changes in mRNA Are Consistent with an EMT and Correlate with Changes in Protein Abundance during Pre-malignant Immortalization

To understand the transition between distinct EMT phenotypic states, we quantified global mRNA and protein abundance in all three cell lines (PRIM, IMO, and TFO). We measured global transcriptomics using

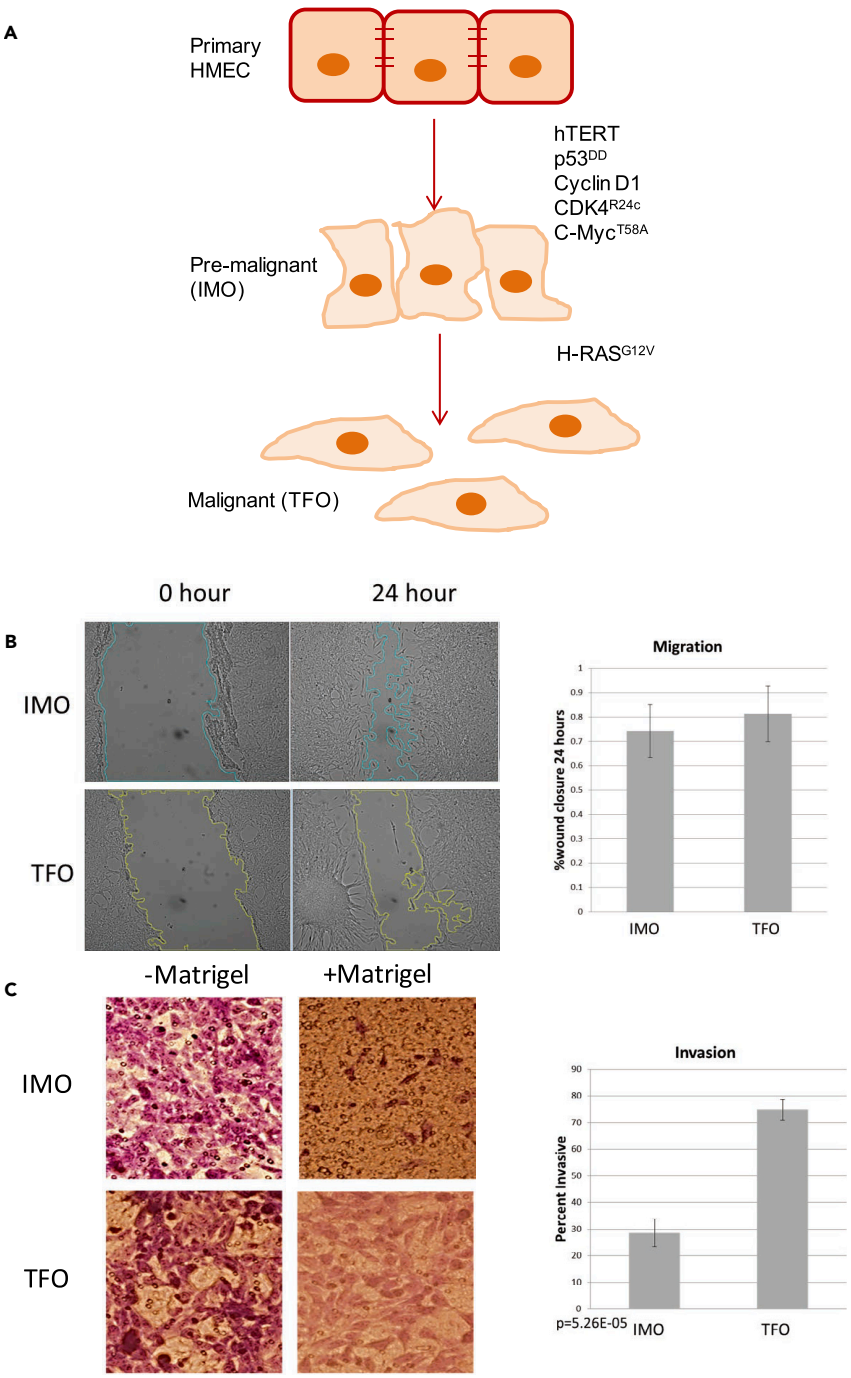

Figure 1. Pre-malignant Immortalized Cells Have a Migratory Phenotype, whereas Ras-transformed Cells Have Increased Invasive Capacity

(A) Genetically defined system of breast cancer progression.

(B) Wound-healing scratch assay: Shown are representative photographs and quantification of scratch closure after 24 hr for four biological replicates. Data are represented as mean ± SEM. SEM, standard error of the mean.

(C) Transwell assay: Shown are representative images and the mean and standard deviation of three biological replicates, quantified as percentage that migrated through Matrigel versus through the control membrane without Matrigel. Data are represented as mean ± SEM.

See also Figure S1

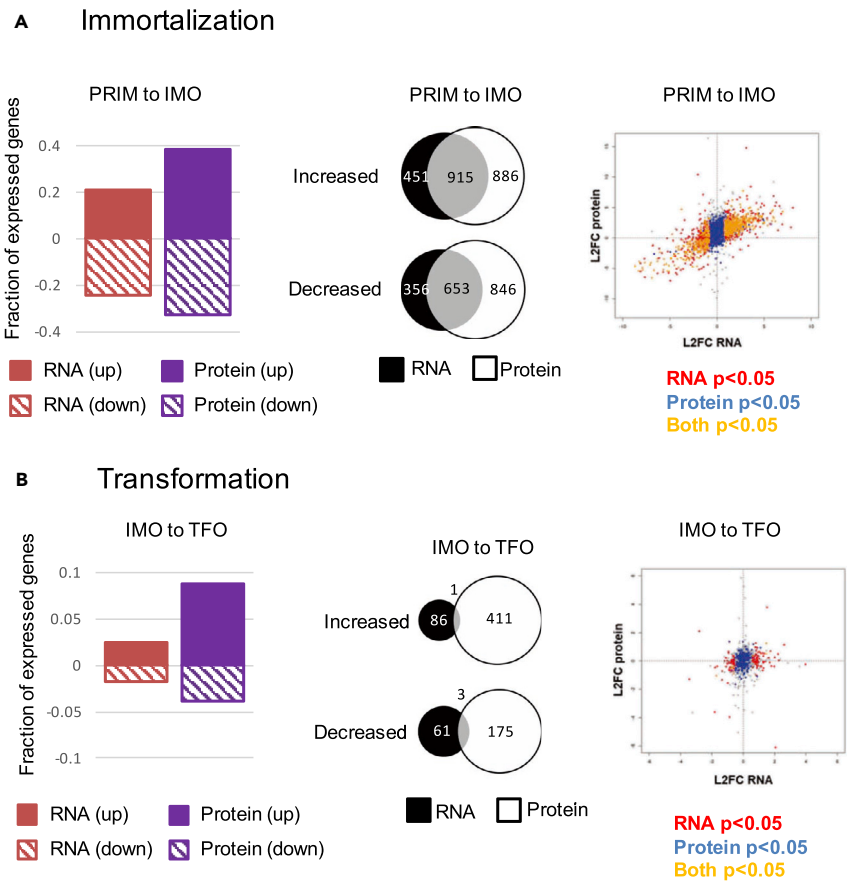

Figure 2. Changes in mRNA and Protein Abundance Correlate during Immortalization, but Not Following Ras Transformation

(Left) Fraction of total expressed genes whose mRNA (red) or protein (purple) significantly increased (solid) or decreased (striped) during (A) immortalization (IMO) or (B) transformation (TFO).

(Middle) Venn diagram of mRNAs and proteins that increased or decreased significantly ($p < 0.05$) during (A) immortalization or (B) transformation. Overlapping area represents genes for which both the mRNA and corresponding proteins changed in the same direction during the indicated transition.

(Right) Log2 fold change (L2FC) of RNA (x axis) plotted against the L2FC of the corresponding proteins (y axis) during (A) immortalization and (B) transformation. Red dots denote significant ($p < 0.05$) changes in RNA only, blue is protein only, and yellow indicates that both RNA and corresponding protein changed significantly.

See also Figures S2 and S3.

paired-end RNA sequencing and global proteomics using quantitative one-dimensional UPLC-MS/MS, both methods in biological triplicate (Table S1).

During the PRIM to IMO transition (also referred to as "immortalization"), we detected extensive changes in both mRNA and protein abundance (Figure 2A, left panel). Many of the mRNAs that changed during immortalization were expected based on the known pathways that were perturbed by the transgenes expressed in these cells (Figure S2A). For example, we saw enrichment for Gene Ontology (GO) categories including "telomere maintenance," "cell proliferation," "mitotic cell cycle process," "chromosome organization," "programmed cell death," and "negative regulation of cell proliferation." Importantly, we also observed enrichment of upregulated mRNAs involved in "epithelial cell migration" and enrichment of downregulated mRNAs involved in "cell adhesion," consistent with our observation that IMO cells are migratory. For about 66% of the mRNAs that changed expression during immortalization, we observed a concordant change in corresponding protein abundance (Figure 2A, middle panel). Globally we observed a strong correlation between changes in mRNAs and corresponding proteins (Figure 2A, right panel). Therefore, changes in proteins that drive migration in these immortalized cells were, in large part, driven by dramatic changes in the transcriptome.

To quantify the interplay between EMT progression and primary cell immortalization, we used a previously published method for EMT scoring based on global RNA abundance signatures (Tan et al., 2014). EMT signature scores were calculated using a two-sample Kolmogorov-Smirnov test based on multiple gene expression signatures and reported as a value between −1 and +1, with more positive scores indicating a more mesenchymal state. PRIM cells had a calculated score of 0.22905 ($p = 0.05737$), indicative of an intermediate or mixed epithelial-mesenchymal RNA signature, and IMO cells had a score of 0.71391 ($p = 2.109 \times 10^{-15}$), indicating a strong mesenchymal signature (Figure S2B).

Transcripts encoding proteins involved in RNA processing were also among the RNAs that increased during the transition from PRIM to IMO, and as a group, core splicing machinery components were significantly upregulated during immortalization (Figure S2C). This observation suggested that, in addition to changes in RNA abundance, immortalization may also cause changes in splicing. Indeed, we observed a large number of significant alternative splicing changes during immortalization (Figure S2D, blue). It has been previously reported that EMT drives an alternative splicing program associated with multiple tumor types (Shapiro et al., 2011; Yang et al., 2016). We therefore assessed the extent of EMT-specific alternative splicing by comparing previously reported EMT splicing signatures with changes observed during the PRIM to IMO transition. We observed close agreement between these datasets (Figures S2E and S2F), and we identified and validated many well-described mesenchymal isoforms, including those for CD44, ENAH (also known as MENA), and p120-catenin, in our system (Figure S3) (Prochazka et al., 2014; Rohan et al., 2014; Sarrio et al., 2004).

In addition to these isoforms that are known to be regulated during EMT, we identified several other splicing events that we would predict to have an impact on cell migration. For example, alternative splicing of Myo1b, which encodes unconventional myosin, yields proteins with lever arms of different lengths that regulate myosin step size and thus, are likely to increase motility rates (Laakso et al., 2010). Expression of this isoform of Myo1b has also been observed in other models of EMT (Yang et al., 2016). We also observed alternative splicing of Discs large homolog 1 (DLG1), a scaffolding protein, in a region that allows interactions with protein kinases, including Crk, which regulates cell adhesion, spreading, and migration (McLaughlin et al., 2002) (Figures S3 and S4). These alternative splicing events are novel in the context of EMT, and our data suggest that they may contribute to a migratory phenotype.

Changes in mRNA Abundance Do Not Correlate with Changes in Protein Abundance during Ras Transformation

In contrast to the transition from PRIM to IMO, very few significant changes in mRNA expression occurred during the IMO to TFO transition (Figure 2B, left panel). This was surprising in light of the drastic difference in anchorage-independent growth and invasiveness (Figure 1C) (Bisogno and Keene, 2017). When we applied the EMT signature scoring system, TFO cells were assigned a score of 0.53635 ($p = 8.02 \times 10^{-8}$) (Figure S2B), indicating that TFO cells have a gene expression signature typical of mesenchymal cells. However, this mRNA expression signature is not more mesenchymal when compared with IMO cells, despite their acquired invasiveness. In addition, the EMT-related alternative splicing events observed during the PRIM to IMO transition were maintained following Ras transformation, but we did not detect any additional changes in alternative splicing (Figures S2C–S2F). However, significantly more proteins were differentially expressed than mRNAs (Figure 2B, left panel). When comparing proteins that changed expression with their corresponding mRNA changes, there was very little overlap and poor correlation (Figure 2B, middle and right panels), suggesting that changes in protein abundance, but not RNA abundance or processing, may be driving changes in malignancy and invasiveness during transformation.

Ras Transformation Enhances the Changes in Protein Expression that Occur during Immortalization

We observed a progression of cellular behavior from IMO cells being more migratory than PRIM to TFO cells being more invasive than IMO, yet the EMT RNA signatures only showed a significant difference in immortalization and not during transformation. We reasoned that changes in protein abundance during transformation were driving the increase in invasion. To investigate how these changes of protein abundance induce migratory cells to become invasive, we compared protein changes during transformation with changes during immortalization. Interestingly, there was good correlation between the liquid chromatography (LC)-MS/MS-derived changes in protein abundance during both transitions, indicating that many proteins that changed during immortalization were altered in the same direction following transformation

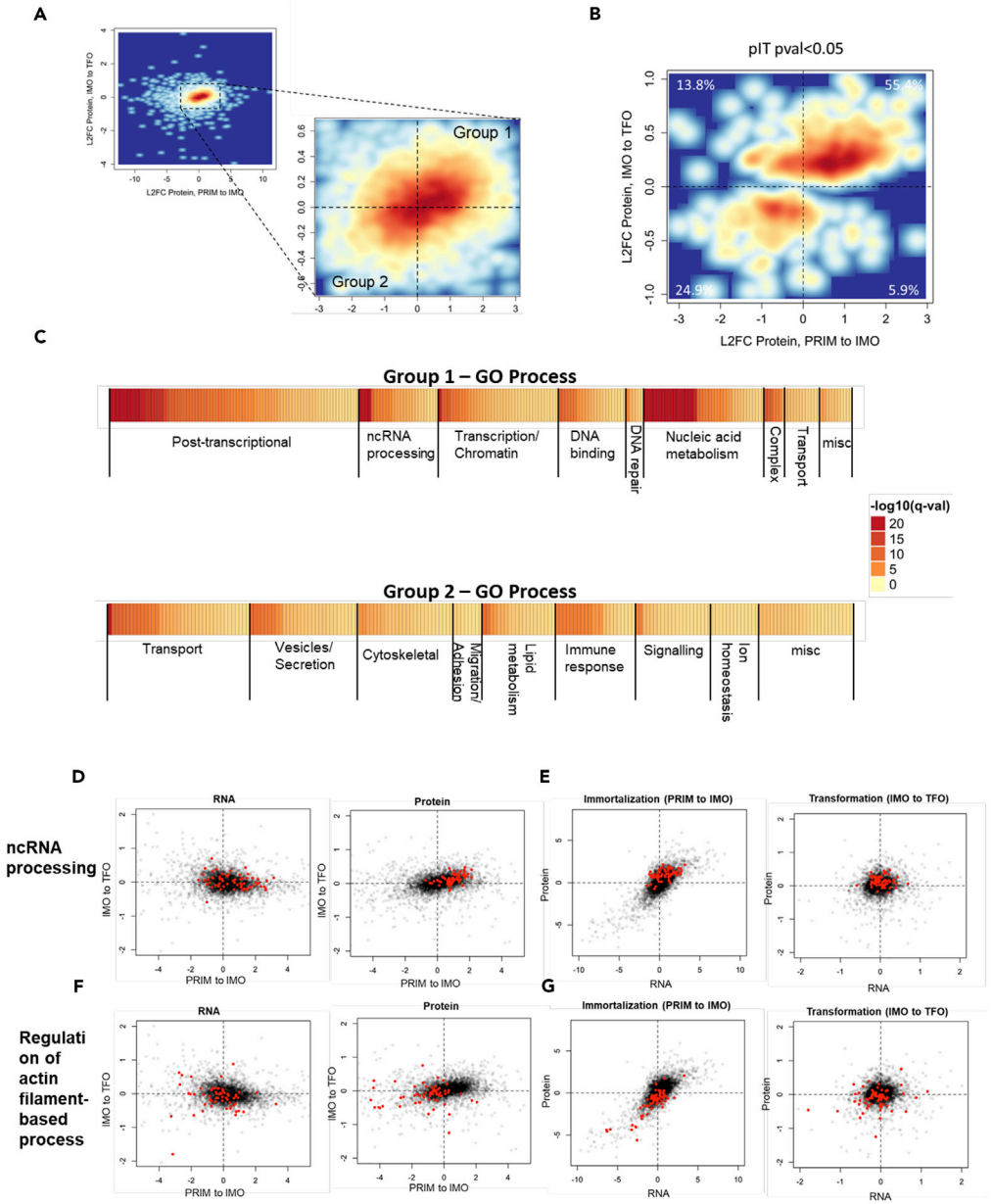

Figure 3. Ras Transformation Enhances the Changes in Protein Expression that Occur during Immortalization

(A) Log2 fold change (L2FC) protein abundance during immortalization (PRIM to IMO, x axis) versus transformation (IMO to TFO, y axis) for all expressed genes. Group 1 includes all proteins that increase, and Group 2 includes all proteins that decrease during both transitions.

(B) L2FC protein abundance during immortalization (PRIM to IMO, x axis) versus transformation (IMO to TFO, y axis) for all expressed genes, filtered for significantly changed proteins ($p < 0.05$) during the IMO to TFO transition (a total of 575 proteins met this criteria). Percent values indicate percentage of proteins contained within each quadrant.

(C) GO process categories for significantly changed proteins in "Group 1" (increased during both transitions) and "Group 2" (decreased during both transitions).

(D) Comparison of L2FC of RNA (left panel) and protein (right panel) during immortalization (x axis) and transformation (y axis) for the ncRNA processing GO category (Group 1).

(E) Comparison of L2FC of RNA (x axis) and protein (y axis) during immortalization (left panel) and transformation (right panel) for the ncRNA processing GO category (Group 1).

Figure 3. *Continued*
(F) Comparison of L2FC RNA (left panel) and protein (right panel) during immortalization (x axis) and transformation (y axis) for the regulation of actin filament-based processes GO category (Group 2).
(G) Comparison of L2FC of RNA (x axis) and protein (y axis) during immortalization (left panel) and transformation (right panel) for the regulation of actin filament-based processes GO category (Group 2).
See also Figure S4.

(Figure 3A, Groups 1 and 2). To see how changes in protein abundance during transformation relate to changes occurring in the preceding PRIM to IMO transition, we filtered the data for all proteins that changed significantly ($p > 0.05$) during Ras transformation and observed that 55.4% of these proteins increased during immortalization and further increased following transformation, whereas 24.9% of the proteins decreased during immortalization and further decreased during transformation (Figure 3B). Thus, less than 20% of all dynamically changing proteins showed opposite changes between immortalization and transformation. This indicates that Ras is primarily enhancing changes in protein abundance that had occurred during the preceding stage of immortalization.

To investigate how these correlating changes relate to the observed phenotypic changes, we grouped proteins according to their changes during immortalization and transformation, with proteins increasing during both transitions belonging to Group 1 and those decreasing during both transitions belonging to Group 2. Among the proteins within each of these groups, we saw enrichment for numerous GO categories falling into eight broad groupings each. For Group 1, the categories fell into the following groupings: "post-transcriptional process," "non-coding RNA processing," "transcription/chromatin," "DNA binding," "DNA repair," "nucleic acid metabolism," "complex," and "transport" (Figure 3C). For Group 2 proteins, the categories fell into the following groupings: "transport," "vesicles/secretion," "lipid metabolism," "immune response," "signaling," "ion homeostasis," and, importantly, "cytoskeletal" and "migration/adhesion" (Figure 3C).

Much like our observed global expression patterns, functional categories of mRNA and protein correlated during immortalization but were not correlated during transformation. For example, proteins involved in non-coding RNA processing (Group 1) increased from PRIM to IMO and then again from IMO to TFO (Figure 3D, right panel), whereas the mRNAs encoding these proteins did not follow the same pattern (Figure 3D, left panel). Both RNA and protein increased during the PRIM to IMO transition (Figure 3E, left panel), whereas only proteins increased during the IMO to TFO transition (Figure 3E, right panel). Similarly, proteins involved in the regulation of actin filament-based processes (Group 2) decreased in abundance from PRIM to IMO and then decreased again from IMO to TFO, whereas the mRNAs encoding these proteins had decreased expression from PRIM to IMO but subsequently did not change, as a group, from IMO to TFO (Figures 3F and 3G). We validated the UPLC-MS/MS data by western blotting and RNA-seq data via qRT-PCR for several Group 1 and Group 2 proteins (Figure S5). Indeed, individual protein levels increased (Figure S5A) or decreased (Figure S5B) during Ras transformation without significant corresponding changes in mRNA. Therefore, although immortalization and transformation appear to cooperate to promote EMT, they do so by distinct mechanisms. Changes in protein expression correlate with changes in mRNA expression during immortalization, suggesting regulation of transcription and/or RNA stability, while oncogenic Ras further enhances these changes in protein abundance with no corresponding changes in RNA expression, suggesting regulation via post-transcriptional mechanisms, such as translation and/or protein stability, during transformation.

Knockdown of α-Adducin Enhances Invasion of Immortalized Cells

Since the enriched GO categories for Group 2 proteins contained many categories related to "cytoskeletal" and "adhesion/migration," suggesting that Ras-driven changes in protein abundance may result in increased invasion, we sought to test whether mimicking these changes in IMO cells could induce the transformation-specific invasive phenotype. As a proof of principle, we examined ADD1, a Group 2 protein. ADD1 is a membrane skeletal protein that plays a role in the formation and stabilization of the membrane cytoskeleton by binding and capping actin filaments and promoting actin association with spectrin (Li et al., 1998). ADD1 has a demonstrated role in maintaining epithelial junction and barrier integrity, and knockdown of ADD1 decreases adherens junctions and tight junction assembly through diminished spectrin recruitment and a decrease in F-actin abundance, resulting in the impaired assembly of actin bundles (Naydenov and Ivanov, 2010).

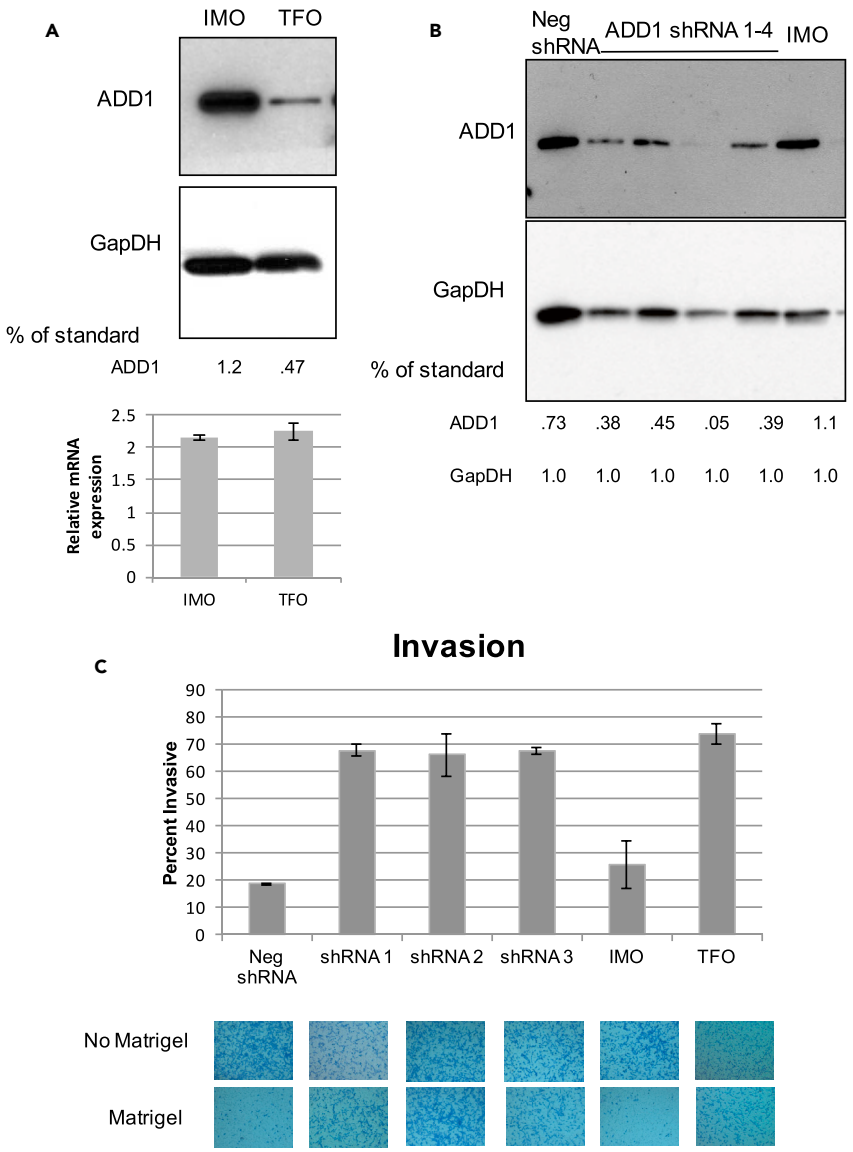

Figure 4. Knockdown of α-Adducin Enhances Invasion of Immortalized Cells

(A) Western blot validation of the LC-MS/MS detected decrease of ADD1 in TFO versus IMO cells and shRNA knockdown of ADD1 in IMO cells.

(B) qRT-PCR of ADD1-encoding mRNA in IMO and TFO cells, shown as relative expression to PRIM cells, normalized to Glyceraldehyde 3-phosphate dehydrogenase (GapDH). Data are represented as mean ± standard deviation, n = 4.

(C) Transwell assay: Shown are representative images and the mean and standard deviation of two biological replicates of each shRNA, six biological replicates of IMO, and four biological replicates of TFO, quantified as percentage that migrated through Matrigel versus through the membrane without Matrigel. Data are represented as the mean ± SEM.

Expression of oncogenic Ras resulted in a decrease in ADD1 protein abundance with no significant change in mRNA expression (Figures 4A and 4B). We reduced the levels of ADD1 in IMO cells using three shRNA constructs (Figure 4A). ADD1 reduction in IMO cells drastically increased cell invasion while having no effect on cell survival, similar to what we observed during Ras transformation (Figure 4C). In summary, ADD1 protein expression levels decreased during immortalization, yet did not lead to an invasive phenotype. ADD1 protein, but not its encoding mRNA, was further reduced in response to oncogenic Ras transformation, and both oncogenic Ras expression and direct knockdown of ADD1 resulted in increased cell invasion.

Therefore, our data suggest that oncogenic Ras induces EMT-associated invasion, at least in part, by directly decreasing the levels of ADD1 protein.

DISCUSSION

EMT Induction and Synergistic Cooperation with Ras

Just as normal cells evolve to a neoplastic state during malignant progression, epithelial cells transition through a series of intermediate stages during the process of EMT. During an EMT, epithelial cells pass through intermediate and reversible states with a mixture of epithelial and mesenchymal properties, and cells in a partial EMT state may simultaneously express epithelial and mesenchymal markers and acquire some EMT-related phenotypes (Nieto et al., 2016). Unlike traditional one-step models of EMT, our genetically defined, stepwise system enabled us to gain novel mechanistic insights into different EMT-intermediate states. In the first stage of primary cell immortalization, we observed a repression of the epithelial gene expression signature, activation of a mesenchymal program, and a dramatic increase in cell migration. Ras transformation of these immortalized cells enhanced the changes laid out during the first stage by enhancing the expression levels of a subset of proteins, resulting in an invasive phenotype. In fact, over 80% of the Ras-induced changes were changed in the same direction up or down during immortalization, suggesting a synergy between the two stages where pre-malignant cells were primed for Ras-triggered activation.

Although the acquisition of most cancer hallmarks can be encompassed into a model of Darwinian evolution in which genetic mutations confer a selective advantage, activation of migration and invasion does not provide an obvious survival advantage to the primary tumor (Gerlinger et al., 2012; Gupta et al., 2005; Hanahan and Weinberg, 2011). Therefore, it has been postulated that mutations that directly contribute to metastatic competence may be harbored within genetic lesions for another trait that renders a selective advantage within the primary tumor (Gupta et al., 2005). Given the cooperation between stages that promote invasion and malignancy in our model (Figures 1 and S2), we speculate that invasive traits may be harbored within multiple mutations, and in some instances, these mutations may be able to act synergistically.

Ras Synergy with Multiple EMT-Promoting Pathways

Our results suggest that oncogenic Ras works cooperatively with the genetic alterations induced during primary cell immortalization to promote EMT-associated invasion. Interestingly, a previous study showed that KRAS suppression in pancreatic cancer cells attenuated transforming growth factor β (TGF-β)-induced upregulation of Snail, a transcription factor involved in EMT (Horiguchi et al., 2009). In addition, expression of the H-Ras^{G12V} transgene in HeLa cells boosted the upregulation of Snail in response to TGF-β, suggesting that TGF-β signaling and Ras cooperate to induce Snail (Horiguchi et al., 2009). Notably, this TGF-β-Ras synergism induced EMT through a distinct mechanism from immortalization in our system, as we did not observe changes to Snail expression. This suggests that Ras can cooperate with multiple, distinct mechanisms to promote EMT.

We observed synergistic regulation by immortalization and Ras transformation for many proteins involved in EMT-related processes, including the canonical mesenchymal markers vimentin and N-cadherin, as well as many cell adhesion and cytoskeleton organization proteins (Figure S5). Our data suggest that Ras may cooperate with the genetic mutations in the immortalized cells to regulate many EMT-related proteins to promote malignancy and invasion. One example is RIO kinase 1 (RIOK1), which increased protein expression following both immortalization and Ras transformation. Interestingly, a recent study revealed that RIOK1 knockdown reduced invasion in Ras-transformed breast, colon, and lung cancer cells, but it did not have the same effect on cells with wild-type Ras (Weinberg et al., 2017). Moreover, knockdown of RIOK1 in immortalized breast cells reduced KRAS transformation efficiency, suggesting a requirement for RIOK1 in the context of oncogenic Ras signaling (Weinberg et al., 2017). Another example of an EMT-related change was Drebrin-like (DBNL) actin-binding protein, which was reduced following both immortalization and Ras transformation. DBNL is necessary for the formation of podosome rosettes (Boateng et al., 2012). Podosomes are dynamic structures that regulate extracellular matrix adhesion and degradation, and knockdown of DBNL in Src-transformed fibroblasts greatly increased invasive cell migration (Boateng et al., 2012). In breast cancer, DBNL has been characterized as a metastatic suppressor, and it is stabilized by the RNA-binding protein MBNL1 (Fish et al., 2016).

Post-transcriptional Mechanisms Triggered by Oncogenic Ras

Although many studies have relied on steady-state mRNA levels as a proxy for gene expression, it has become increasingly clear that mRNA levels alone do not provide a complete picture of the complex regulatory processes occurring during cancer cell progression, as evidenced by the fact that steady-state protein levels often do not correlate with steady-state mRNA levels (Griffin et al., 2002; Ideker et al., 2001; Keene, 2001; Mansfield and Keene, 2009). Our global datasets suggest that Ras likely controls invasion through post-transcriptional mechanisms, such as translation and/or protein stability (Figure 2).

Ras signaling has previously been shown to regulate translation. In glioblastoma, Ras and Akt signaling have minimal effects on RNA abundance, whereas they significantly alter mRNA translation (Rajasekhar et al., 2003). Ras signaling is also required for phosphorylation of RPS6 and is thereby involved in stimulating cap-dependent translation (Roux et al., 2007). Furthermore, Ras is required for mitogen-induced phosphorylation of the cap-binding protein eIF4E, thus regulating translation initiation (Frederickson et al., 1992). eIF4E is also known to be phosphorylated during TGF-β-induced EMT, which in turn regulates translation of Snail and Mmp-3 (Robichaud et al., 2015).

In addition to directly regulating the translational machinery, Ras can regulate the activity of sequence-specific RNA-binding proteins, which bind to elements located in regulatory regions of mRNA, such as 3′ or 5′ untranslated regions (UTRs), and regulate the translation of multiple functionally related genes, or RNA regulons. For example, the CELF6 RNA-binding protein has been demonstrated to rescue KRAS suppression in oncogene-addicted cells (Shao et al., 2014). Furthermore, a recent study established a role for CELF1, a related family member of CELF6, in regulating EMT-associated translational regulation (Chaudhury et al., 2016). Several other studies have demonstrated roles for translational RNA regulons in the acquisition of cancer-related phenotypes downstream of major oncogenic signaling pathways (Jung et al., 2014; Romeo et al., 2013; Shahbazian et al., 2010; Truitt and Ruggero, 2016; Tsukumo et al., 2016; Wurth et al., 2016).

Regulation of protein localization and turnover also greatly determines cellular processes. EMT is regulated by post-translational modifications that can influence protein localization and degradation. For example, Snail is phosphorylated by glycogen synthase kinase (GSK)-3β, leading to nuclear export and subsequent ubiquitin-mediated proteasome degradation, whereas dephosphorylation by SCP inhibits Snail degradation (Wu et al., 2009; Zhou et al., 2004). Ras signaling can lead to the activation of mitogen-activated protein kinases (MAPK), which phosphorylates downstream targets involved in cancer progression and EMT. MAPK-mediated phosphorylation of the transcription factor TWIST1 increased protein levels without affecting mRNA levels, leading to breast cancer cell invasiveness (Hong et al., 2011). Furthermore, the Ras-ERK MAPK signaling pathway has been demonstrated to inhibit the ubiquitin-proteasome pathway in both developing T cells and during mitogen activation of fibroblasts (Sears et al., 1999; Yamashita et al., 2005). Interestingly, our data showed upregulation of components of the anaphase-promoting complex/cyclosome (APC/C), including Bub1B, CDC20, UBE2C, and UBE2S (Table S1). The APC/C is a ubiquitin ligase complex that regulates a variety of cellular processes, including invasion, by targeting different substrates for ubiquitination (Zhou et al., 2016). It is therefore possible that a number of the proteins that are decreased in response to oncogenic Ras could be targeted for ubiquitination by the APC/C complex.

In summary, we have identified a novel and synergistic transition in gene expression whereby mutated oncogenic Ras post-transcriptionally enhances changes primed via genetic mutations in pre-malignant cells, resulting in a significant increase in malignancy and cell invasiveness. This work provides important insights into the mechanisms by which cancer-associated genetic mutations cooperate to promote transitions through partial EMT states.

METHODS

All methods can be found in the accompanying Transparent Methods supplemental file.

SUPPLEMENTAL INFORMATION

Supplemental Information includes Transparent Methods, five figures, and six tables and can be found with this article online at https://doi.org/10.1016/j.isci.2018.05.011.

ACKNOWLEDGMENTS

We thank Jeff Blackinton, Kyle Mansfield, and Cindo Nicholson for helpful discussions and critical insights. We also thank Duke University's Center for Genomic and Computational Biology, as well as Matt Foster and Will Thompson at Duke University's Proteomics Core Facility. This work was funded by grants from the NIH: R01CA157268 (J.D.K.) and F31CA185892 (L.S.B.).

AUTHOR CONTRIBUTIONS

Conceptualization, J.D.K., L.S.B., and M.B.F.; Methodology, L.S.B., M.B.F., and J.D.K.; Formal Analysis, L.S.B. and M.B.F.; Investigation, L.S.B.; Resources, J.D.K.; Data Curation, M.B.F.; Writing – Original Draft, Review, & Editing, L.S.B., M.B.F., and J.D.K.; Visualization, L.S.B. and M.B.F.; Funding Acquisition, J.D.K. and L.S.B.

DECLARATION OF INTERESTS

The authors declare no conflict of interest.

Received: July 21, 2017
Revised: February 12, 2018
Accepted: May 15, 2018
Published: June 29, 2018

REFERENCES

Bisogno, L.S., and Keene, J.D. (2017). Analysis of post-transcriptional regulation during cancer progression using a donor-derived isogenic model of tumorigenesis. Methods *126*, 193–200.

Boateng, L.R., Cortesio, C.L., and Huttenlocher, A. (2012). Src-mediated phosphorylation of mammalian Abp1 (DBNL) regulates podosome rosette formation in transformed fibroblasts. J. Cell Sci. *125*, 1329–1341.

Chaudhury, A., Cheema, S., Fachini, J.M., Kongchan, N., Lu, G., Simon, L.M., Wang, T., Mao, S., Rosen, D.G., Ittmann, M.M., et al. (2016). CELF1 is a central node in post-transcriptional regulatory programmes underlying EMT. Nat. Commun. *7*, 13362.

Fish, L., Pencheva, N., Goodarzi, H., Tran, H., Yoshida, M., and Tavazoie, S.F. (2016). Muscleblind-like 1 suppresses breast cancer metastatic colonization and stabilizes metastasis suppressor transcripts. Genes Dev. *30*, 386–398.

Frederickson, R.M., Mushynski, W.E., and Sonenberg, N. (1992). Phosphorylation of translation initiation factor eIF-4E is induced in a ras-dependent manner during nerve growth factor-mediated PC12 cell differentiation. Mol. Cell Biol. *12*, 1239–1247.

Gerlinger, M., Rowan, A.J., Horswell, S., Larkin, J., Endesfelder, D., Gronroos, E., Martinez, P., Matthews, N., Stewart, A., Tarpey, P., et al. (2012). Intratumor heterogeneity and branched evolution revealed by multiregion sequencing. N. Engl. J. Med. *366*, 883–892.

Griffin, T.J., Gygi, S.P., Ideker, T., Rist, B., Eng, J., Hood, L., and Aebersold, R. (2002). Complementary profiling of gene expression at the transcriptome and proteome levels in *Saccharomyces cerevisiae*. Mol. Cell Proteomics *1*, 323–333.

Gupta, P.B., Mani, S., Yang, J., Hartwell, K., and Weinberg, R.A. (2005). The evolving portrait of cancer metastasis. Cold Spring Harb. Symp. Quant. Biol. *70*, 291–297.

Hahn, W.C., Counter, C.M., Lundberg, A.S., Beijersbergen, R.L., Brooks, M.W., and Weinberg, R.A. (1999). Creation of human tumour cells with defined genetic elements. Nature *400*, 464–468.

Hanahan, D., and Weinberg, R.A. (2011). Hallmarks of cancer: the next generation. Cell *144*, 646–674.

Hong, J., Zhou, J., Fu, J., He, T., Qin, J., Wang, L., Liao, L., and Xu, J. (2011). Phosphorylation of serine 68 of Twist1 by MAPKs stabilizes Twist1 protein and promotes breast cancer cell invasiveness. Cancer Res. *71*, 3980–3990.

Horiguchi, K., Shirakihara, T., Nakano, A., Imamura, T., Miyazono, K., and Saitoh, M. (2009). Role of Ras signaling in the induction of snail by transforming growth factor-beta. J. Biol. Chem. *284*, 245–253.

Husemann, Y., Geigl, J.B., Schubert, F., Musiani, P., Meyer, M., Burghart, E., Forni, G., Eils, R., Fehm, T., Riethmuller, G., et al. (2008). Systemic spread is an early step in breast cancer. Cancer Cell *13*, 58–68.

Ideker, T., Thorsson, V., Ranish, J.A., Christmas, R., Buhler, J., Eng, J.K., Bumgarner, R., Goodlett, D.R., Aebersold, R., and Hood, L. (2001). Integrated genomic and proteomic analyses of a systematically perturbed metabolic network. Science *292*, 929–934.

Jung, H., Gkogkas, C.G., Sonenberg, N., and Holt, C.E. (2014). Remote control of gene function by local translation. Cell *157*, 26–40.

Keene, J.D. (2001). Ribonucleoprotein infrastructure regulating the flow of genetic information between the genome and the proteome. Proc. Natl. Acad. Sci. USA *98*, 7018–7024.

Kendall, S.D., Adam, S.J., and Counter, C.M. (2006). Genetically engineered human cancer models utilizing mammalian transgene expression. Cell Cycle *5*, 1074–1079.

Kendall, S.D., Linardic, C.M., Adam, S.J., and Counter, C.M. (2005). A network of genetic events sufficient to convert normal human cells to a tumorigenic state. Cancer Res. *65*, 9824–9828.

Laakso, J.M., Lewis, J.H., Shuman, H., and Ostap, E.M. (2010). Control of myosin-I force sensing by alternative splicing. Proc. Natl. Acad. Sci. USA *107*, 698–702.

Lambert, A.W., Pattabiraman, D.R., and Weinberg, R.A. (2017). Emerging biological principles of metastasis. Cell *168*, 670–691.

Lamouille, S., Xu, J., and Derynck, R. (2014). Molecular mechanisms of epithelial-mesenchymal transition. Nat. Rev. Mol. Cell Biol. *15*, 178–196.

Li, X., Matsuoka, Y., and Bennett, V. (1998). Adducin preferentially recruits spectrin to the fast growing ends of actin filaments in a complex requiring the MARCKS-related domain and a newly defined oligomerization domain. J. Biol. Chem. *273*, 19329–19338.

Mani, S.A., Guo, W., Liao, M.J., Eaton, E.N., Ayyanan, A., Zhou, A.Y., Brooks, M., Reinhard, F., Zhang, C.C., Shipitsin, M., et al. (2008). The epithelial-mesenchymal transition generates cells with properties of stem cells. Cell *133*, 704–715.

Mansfield, K.D., and Keene, J.D. (2009). The ribonome: a dominant force in co-ordinating gene expression. Biol. Cell *101*, 169–181.

McLaughlin, M., Hale, R., Ellston, D., Gaudet, S., Lue, R.A., and Viel, A. (2002). The distribution and function of alternatively spliced insertions in hDlg. J. Biol. Chem. *277*, 6406–6412.

Naydenov, N.G., and Ivanov, A.I. (2010). Adducins regulate remodeling of apical junctions in human epithelial cells. Mol. Biol. Cell *21*, 3506–3517.

Nieto, M.A., Huang, R.Y., Jackson, R.A., and Thiery, J.P. (2016). Emt: 2016. Cell *166*, 21–45.

Podsypanina, K., Du, Y.C., Jechlinger, M., Beverly, L.J., Hambardzumyan, D., and Varmus, H. (2008). Seeding and propagation of untransformed mouse mammary cells in the lung. Science *321*, 1841–1844.

Prochazka, L., Tesarik, R., and Turanek, J. (2014). Regulation of alternative splicing of CD44 in cancer. Cell. Signal. *26*, 2234–2239.

Rajasekhar, V.K., Viale, A., Socci, N.D., Wiedmann, M., Hu, X., and Holland, E.C. (2003). Oncogenic Ras and Akt signaling contribute to glioblastoma formation by differential recruitment of existing mRNAs to polysomes. Mol. Cell *12*, 889–901.

Rhim, A.D., Mirek, E.T., Aiello, N.M., Maitra, A., Bailey, J.M., McAllister, F., Reichert, M., Beatty, G.L., Rustgi, A.K., Vonderheide, R.H., et al. (2012). EMT and dissemination precede pancreatic tumor formation. Cell *148*, 349–361.

Robichaud, N., del Rincon, S.V., Huor, B., Alain, T., Petruccelli, L.A., Hearnden, J., Goncalves, C., Grotegut, S., Spruck, C.H., Furic, L., et al. (2015). Phosphorylation of eIF4E promotes EMT and metastasis via translational control of SNAIL and MMP-3. Oncogene *34*, 2032–2042.

Rohan, T.E., Xue, X., Lin, H.M., D'Alfonso, T.M., Ginter, P.S., Oktay, M.H., Robinson, B.D., Ginsberg, M., Gertler, F.B., Glass, A.G., et al. (2014). Tumor microenvironment of metastasis and risk of distant metastasis of breast cancer. J. Natl. Cancer Inst. *106*, https://doi.org/10.1093/jnci/dju136.

Romeo, Y., Moreau, J., Zindy, P.J., Saba-El-Leil, M., Lavoie, G., Dandachi, F., Baptissart, M., Borden, K.L., Meloche, S., and Roux, P.P. (2013). RSK regulates activated BRAF signalling to mTORC1 and promotes melanoma growth. Oncogene *32*, 2917–2926.

Roux, P.P., Shahbazian, D., Vu, H., Holz, M.K., Cohen, M.S., Taunton, J., Sonenberg, N., and Blenis, J. (2007). RAS/ERK signaling promotes site-specific ribosomal protein S6 phosphorylation via RSK and stimulates cap-dependent translation. J. Biol. Chem. *282*, 14056–14064.

Sarrio, D., Perez-Mies, B., Hardisson, D., Moreno-Bueno, G., Suarez, A., Cano, A., Martinez-Perez, J., Gamallo, C., and Palacios, J. (2004). Cytoplasmic localization of p120ctn and E-cadherin loss characterize lobular breast carcinoma from preinvasive to metastatic lesions. Oncogene *23*, 3272–3283.

Sears, R., Leone, G., DeGregori, J., and Nevins, J.R. (1999). Ras enhances Myc protein stability. Mol. Cell *3*, 169–179.

Shahbazian, D., Parsyan, A., Petroulakis, E., Hershey, J., and Sonenberg, N. (2010). eIF4B controls survival and proliferation and is regulated by proto-oncogenic signaling pathways. Cell Cycle *9*, 4106–4109.

Shao, D.D., Xue, W., Krall, E.B., Bhutkar, A., Piccioni, F., Wang, X., Schinzel, A.C., Sood, S., Rosenbluh, J., Kim, J.W., et al. (2014). KRAS and YAP1 converge to regulate EMT and tumor survival. Cell *158*, 171–184.

Shapiro, I.M., Cheng, A.W., Flytzanis, N.C., Balsamo, M., Condeelis, J.S., Oktay, M.H., Burge, C.B., and Gertler, F.B. (2011). An EMT-driven alternative splicing program occurs in human breast cancer and modulates cellular phenotype. PLoS Genet. *7*, e1002218.

Shibue, T., and Weinberg, R.A. (2017). EMT, CSCs, and drug resistance: the mechanistic link and clinical implications. Nat. Rev. Clin. Oncol. *14*, 611–629.

Tan, T.Z., Miow, Q.H., Miki, Y., Noda, T., Mori, S., Huang, R.Y., and Thiery, J.P. (2014). Epithelial-mesenchymal transition spectrum quantification and its efficacy in deciphering survival and drug responses of cancer patients. EMBO Mol. Med. *6*, 1279–1293.

Truitt, M.L., and Ruggero, D. (2016). New frontiers in translational control of the cancer genome. Nat. Rev. Cancer *16*, 288–304.

Tsukumo, Y., Alain, T., Fonseca, B.D., Nadon, R., and Sonenberg, N. (2016). Translation control during prolonged mTORC1 inhibition mediated by 4E-BP3. Nat. Commun. *7*, 11776.

Warzecha, C.C., Jiang, P., Amirikian, K., Dittmar, K.A., Lu, H., Shen, S., Guo, W., Xing, Y., and Carstens, R.P. (2010). An ESRP-regulated splicing programme is abrogated during the epithelial-mesenchymal transition. EMBO J. *29*, 3286–3300.

Weinberg, F., Reischmann, N., Fauth, L., Taromi, S., Mastroianni, J., Kohler, M., Halbach, S., Becker, A.C., Deng, N., Schmitz, T., et al. (2017). The atypical kinase RIOK1 promotes tumor growth and invasive behavior. EBioMedicine *20*, 79–97.

Wu, Y., Evers, B.M., and Zhou, B.P. (2009). Small C-terminal domain phosphatase enhances snail activity through dephosphorylation. J. Biol. Chem. *284*, 640–648.

Wurth, L., Papasaikas, P., Olmeda, D., Bley, N., Calvo, G.T., Guerrero, S., Cerezo-Wallis, D., Martinez-Useros, J., Garcia-Fernandez, M., Huttelmaier, S., et al. (2016). UNR/CSDE1 drives a post-transcriptional program to promote melanoma invasion and metastasis. Cancer Cell *30*, 694–707.

Yamashita, M., Shinnakasu, R., Asou, H., Kimura, M., Hasegawa, A., Hashimoto, K., Hatano, N., Ogata, M., and Nakayama, T. (2005). Ras-ERK MAPK cascade regulates GATA3 stability and Th2 differentiation through ubiquitin-proteasome pathway. J. Biol. Chem. *280*, 29409–29419.

Yang, Y., Park, J.W., Bebee, T.W., Warzecha, C.C., Guo, Y., Shang, X., Xing, Y., and Carstens, R.P. (2016). Determination of a comprehensive alternative splicing regulatory network and combinatorial regulation by key factors during the epithelial-to-mesenchymal transition. Mol. Cell Biol. *36*, 1704–1719.

Yu, M., Bardia, A., Wittner, B.S., Stott, S.L., Smas, M.E., Ting, D.T., Isakoff, S.J., Ciciliano, J.C., Wells, M.N., Shah, A.M., et al. (2013). Circulating breast tumor cells exhibit dynamic changes in epithelial and mesenchymal composition. Science *339*, 580–584.

Zhou, B.P., Deng, J., Xia, W., Xu, J., Li, Y.M., Gunduz, M., and Hung, M.C. (2004). Dual regulation of Snail by GSK-3beta-mediated phosphorylation in control of epithelial-mesenchymal transition. Nat. Cell Biol. *6*, 931–940.

Zhou, Z., He, M., Shah, A.A., and Wan, Y. (2016). Insights into APC/C: from cellular function to diseases and therapeutics. Cell Div. *11*, 9.

ISCI, Volume *4*

Supplemental Information

Ras Post-transcriptionally Enhances a Pre-malignantly Primed EMT to Promote Invasion

Laura S. Bisogno, Matthew B. Friedersdorf, and Jack D. Keene

Supplemental Information:

Supplemental Figures and Legends:

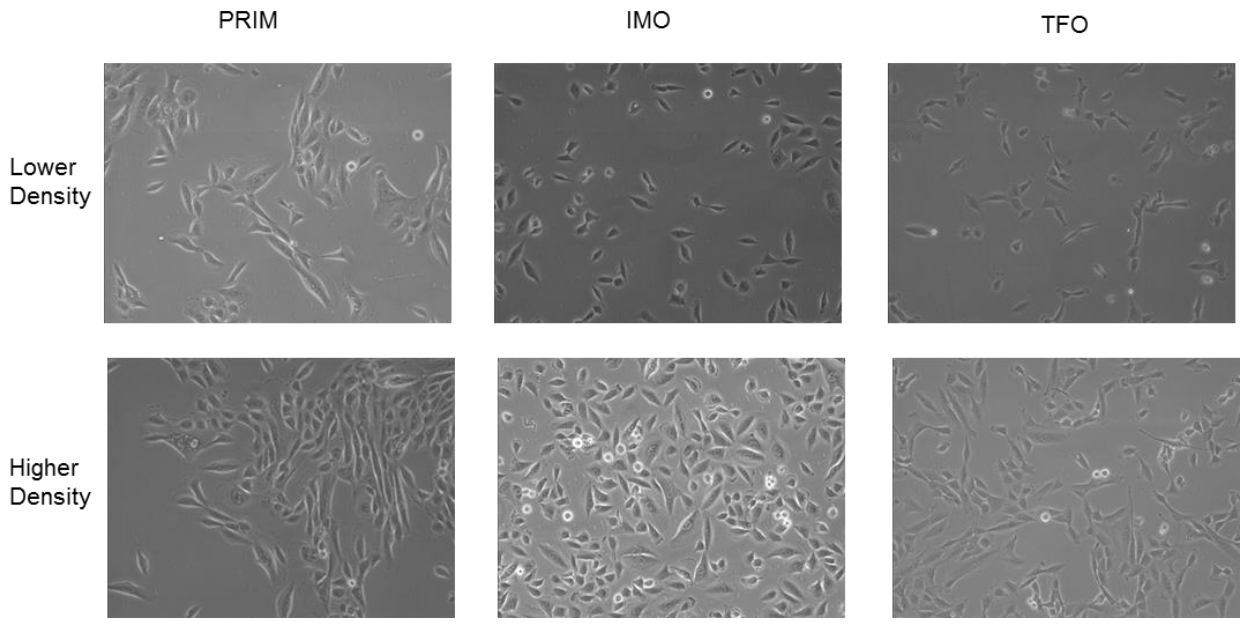

Supplemental Figure 1:
PRIM cells are epithelial, while IMO and TFO cells are morphologically more mesenchymal. Related to Figure 1. Phase contrast micrographs of Primary (PRIM), Immortalized (IMO), and Transformed (TFO) HMECs at low confluency (top) and high confluency (bottom).

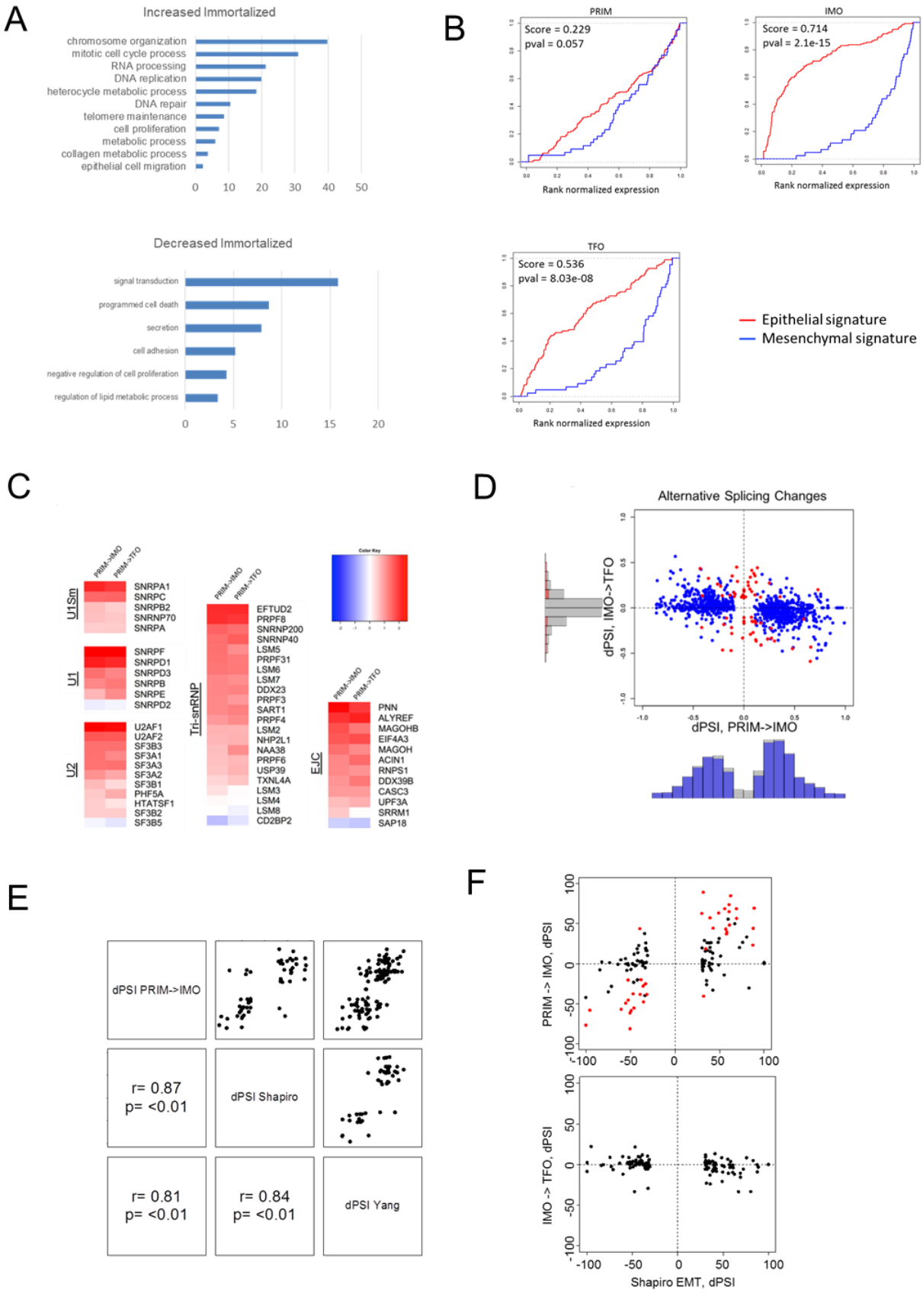
A
Increased Immortalized
chromosome organization
mitotic cell cycle process
RNA processing
DNA replication
heterocycle metabolic process
DNA repair
telomere maintenance
cell proliferation
metabolic process
collagen metabolic process
epithelial cell migration
0 10 20 30 40 50
Decreased Immortalized
signal transduction
programmed cell death
secretion
cell adhesion
negative regulation of cell proliferation
regulation of lipid metabolic process
0 5 10 15 20
B
PRIM
Score = 0.229
pval = 0.057
Rank normalized expression
IMO
Score = 0.714
pval = 2.1e-15
Rank normalized expression
TFO
Score = 0.536
pval = 8.03e-08
Rank normalized expression
Epithelial signature
Mesenchymal signature
C
PRIM->IMO
PRIM->TFO
U1Sm
SNRPA1
SNRPC
SNRPB2
SNRNP70
SNRPA
U1
SNRPF
SNRPD1
SNRPD3
SNRPB
SNRPE
SNRPD2
U2
U2AF1
U2AF2
SF3B3
SF3A1
SF3A3
SF3A2
SF3B1
PHF5A
HTATSF1
SF3B2
SF3B5
Tri-snRNP
EFTUD2
PRPF8
SNRNP200
SNRNP40
LSM5
PRPF31
LSM6
LSM7
DDX23
PRPF3
SART1
PRPF4
LSM2
NHP2L1
NAA38
PRPF6
USP39
TXNL4A
LSM3
LSM4
LSM8
CD2BP2
EJC
PNN
ALYREF
MAGOHB
EIF4A3
MAGOH
ACIN1
RNPS1
DDX39B
CASC3
UPF3A
SRRM1
SAP18
D
Alternative Splicing Changes
dPSI, IMO->TFO
dPSI, PRIM->IMO
E
dPSI PRIM->IMO
r= 0.87
p= <0.01
dPSI Shapiro
r= 0.81
p= <0.01
r= 0.84
p= <0.01
dPSI Yang
F
PRIM -> IMO, dPSI
IMO -> TFO, dPSI
Shapiro EMT, dPSI

Supplemental Figure 2:
IMO cells have a mesenchymal mRNA expression and alternative splicing signatures that are maintained in TFO cells. Related to Figure 2.

A) Enriched GO categories for genes increasing (upper group) or decreasing (lower group) during primary cell immortalization.

B) Previously reported epithelial and mesenchymal gene expression signatures (Tan et al. 2014) were used to generate empirical distribution functions for PRIM, IMO and TFO cells. The X-axis shows ranked normalized expression, with "1" being the most abundant and "0" being the least abundant. EMT signature scores for PRIM, IMO and TFO HMECs were calculated using a two-sample Kolmogorov-Smirnov test. The EMT signature score is reported as a value between -1 and +1, with more positive scores indicating a more mesenchymal state.

C) Expression of mRNA encoding core splicing components increase significantly during immortalization. Heatmap depicts changes from PRIM to IMO and from PRIM to TFO.

D) Significant changes in alternative splicing are observed during immortalization. dPSI= change in percent spliced in. Blue is significant reproducible alternative splicing events from PRIM to IMO and red is significant reproducible alternative splicing events from IMO to TFO.

E) Pair-wise comparison of alternative splicing changes induced during immortalization to previously reported EMT-signatures (Shapiro et al. 2011; Yang et al. 2016). R-values indicate correlation coefficients for each comparison. Top middle box is the comparison between immortalization and Shapiro et al. 2011, R=0.87. Top right box is the comparison between immortalization and Yang et al. 2016, R=0.81. Middle right box is the comparison between Shapiro et al. 2011 and Yang et al. 2016, R=0.84.

F) Comparison of alternative splicing events reported by Shapiro et al. to immortalization (top) and transformation (bottom).

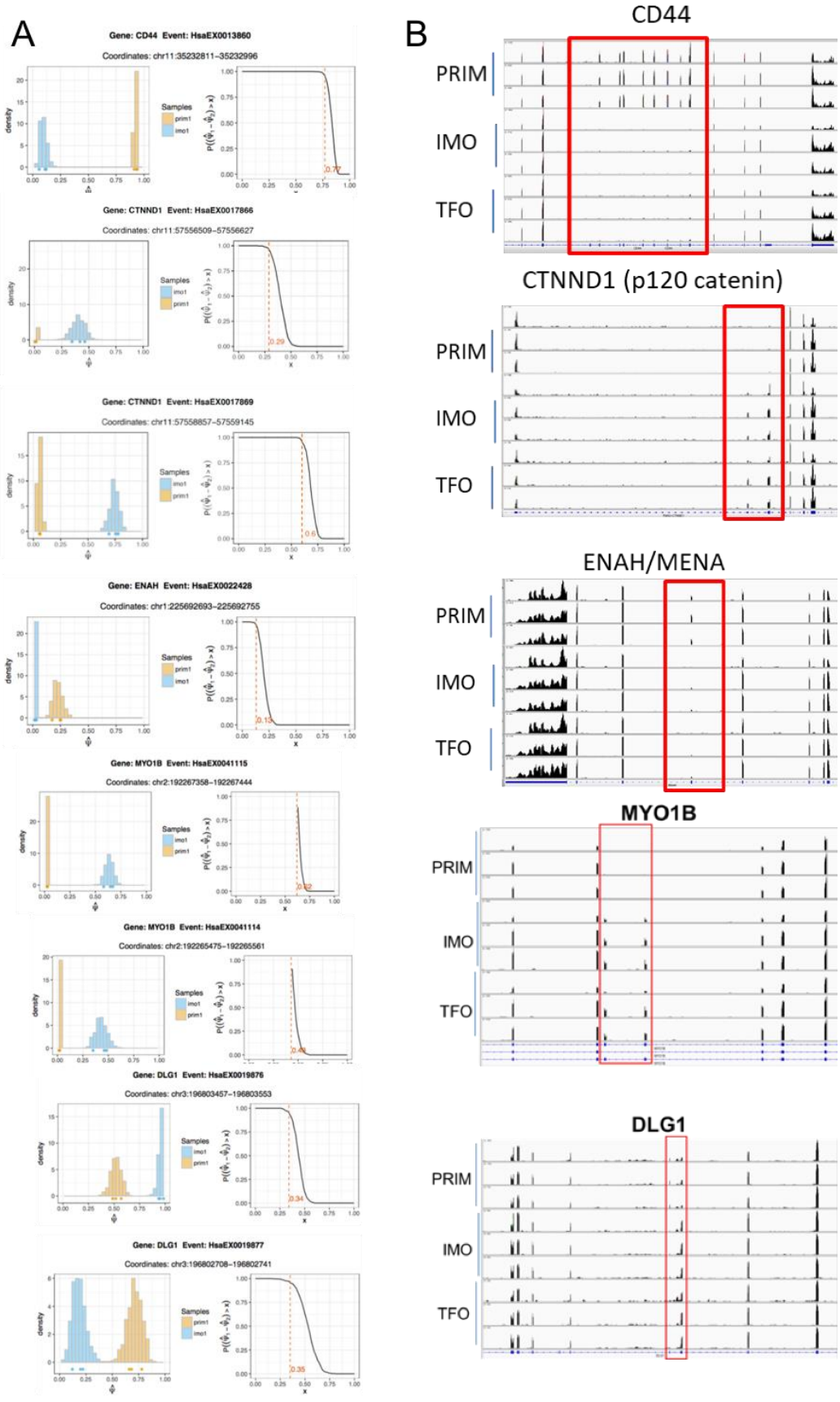
A
Gene: CD44 Event: HsaEX0013860
Coordinates: chr11:35232811−35232996
Gene: CTNND1 Event: HsaEX0017866
Coordinates: chr11:57556509−57556627
Gene: CTNND1 Event: HsaEX0017869
Coordinates: chr11:57558857−57559145
Gene: ENAH Event: HsaEX0022428
Coordinates: chr1:225692693−225692755
Gene: MYO1B Event: HsaEX0041115
Coordinates: chr2:192267358−192267444
Gene: MYO1B Event: HsaEX0041114
Coordinates: chr2:192265475−192265561
Gene: DLG1 Event: HsaEX0019876
Coordinates: chr3:196803457−196803553
Gene: DLG1 Event: HsaEX0019877
Coordinates: chr3:196802708−196802741
Samples
prim1
imo1
density
B
CD44
CTNND1 (p120 catenin)
ENAH/MENA
MYO1B
DLG1
PRIM
IMO
TFO

Supplemental Figure 3:
Visualization and confirmation of well-described (CD44, CTNND1 and ENAH) and novel (Myo1b and DLG1) alternative splicing events during EMT. Related to Figure 2.

A) Visualizations of VAST analysis. The plots in the left panels show the two joint posterior distributions over psi. Each replicate is plotted as dots below the histogram. The right panels show the probability (y-axis) of delta psi being greater than a given value (x-axis). The red line is the 95% confidence interval.

B) IGV screen shots of alternative splicing events, indicated by red boxes.

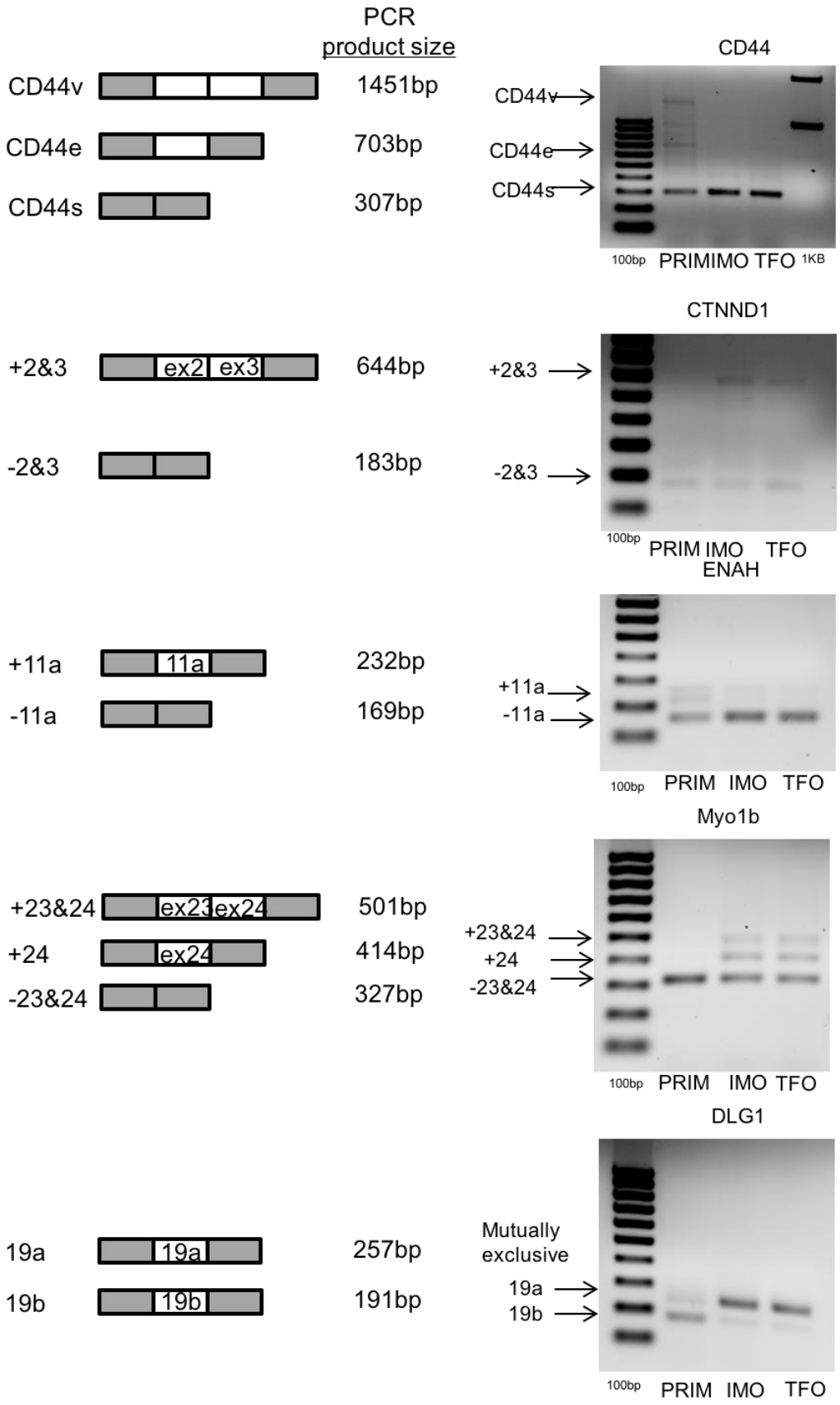
PCR
product size
CD44v
1451bp
CD44e
703bp
CD44s
307bp
CD44
CD44v
CD44e
CD44s
100bp PRIMIMO TFO 1KB
+2&3
ex2 ex3
644bp
-2&3
183bp
CTNND1
+2&3
-2&3
100bp PRIM IMO TFO
ENAH
+11a
11a
232bp
-11a
169bp
+11a
-11a
100bp PRIM IMO TFO
Myo1b
+23&24
ex23ex24
501bp
+24
ex24
414bp
-23&24
327bp
+23&24
+24
-23&24
100bp PRIM IMO TFO
DLG1
19a
19a
257bp
19b
19b
191bp
Mutually
exclusive
19a
19b
100bp PRIM IMO TFO

Supplemental Figure 4:
PCR confirmation of alternative splicing events. Related to Figure 2.

Splice products depiction, name and expected size. PCR validation of alternative splicing events in PRIM, IMO, and TFO cells.

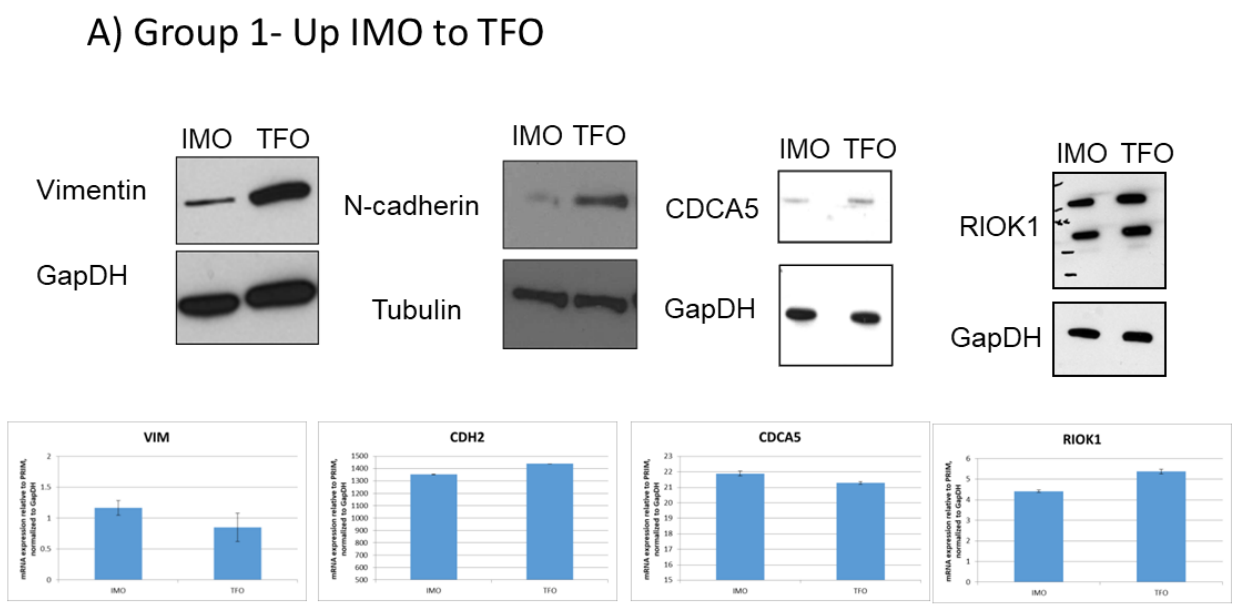

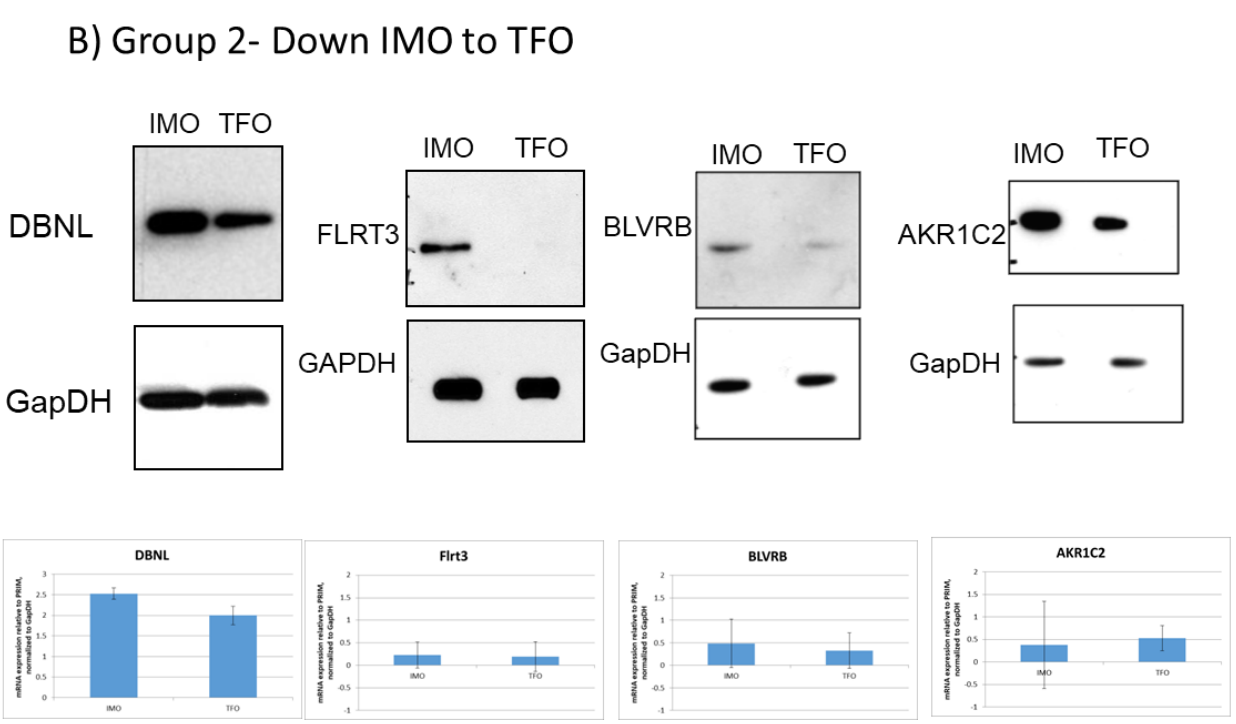

Supplemental Figure 5:
Ras-transformation alters expression of proteins involved in EMT-related processes without altering corresponding mRNA levels. Related to Figures 3 and 4.

Western blot validation of candidate Ras-regulated proteins identified by global proteomics data and qRT-PCR validation of RNA-seq data for mRNAs encoding Ras-regulated proteins that A) increase or B) decrease in protein but not mRNA abundance during oncogenic-Ras transformation.

Transparent Methods:

Cell Culture

HMECs were obtained from Lonza at p9 and maintained in Mammary Epithelial Growth Medium (MEGM; Lonza, Walkersville, MD, USA). IMO and TFO HMECs were maintained in MEGM+10% fetal bovine serum (FBS). Cells were passaged at 50-70% confluency using a Reagent Pack (Lonza) according to the manufacturer's subculturing protocol. All HMECs were authenticated by analysis at the Duke University DNA Analysis Facility. Cells were immortalized and transformed as previously described(Bisogno and Keene, 2017) (Bisogno and Keene, 2017); also see Supplemental Experimental Procedures. 293T/17 packaging cells were obtained from the Duke University Cell Culture Facility and maintained in Dulbecco's Modified Eagle's Medium (ThermoFisher Scientific, Grand Island, NY, USA) +10% FBS. All cells tested mycoplasma negative.

Wound healing scratch assay

Cells were grown in a single monolayer in 6-well plates. Cells were serum starved overnight and during experiment to control for proliferation. A single scratch was made with a p200 pipette tip and the scratch was photographed in 3 distinct places. After 24 hours the scratch was imaged in the same 3 locations, and percent wound closure was quantified using ImageJ's MRI wound healing tool. Data is reported as the mean and standard deviation of 4 replicates.

Matrigel Invasion Assay

Matrigel membrane matrix (Corning, Corning, NY, USA), was thawed on ice overnight and diluted to 300ug/ml in cold coating buffer (0.01M Tris pH 8, 0.7% NaCl, filtered). 100ul of Matrigel was added to 6.5mm Transwell with 8.0um Polycarbonate membrane inserts (Corning), and allowed to solidify at 37C for 2-4 hours. Cells were harvested with Trypsin/EDTA, washed 3 times with serum free media, and resuspended in serum free media at ~50,000 cells/ml. 500ul of cell suspension was added to the upper chamber. 750ul of media with serum was added to the lower chamber. No Matrigel control inserts were used in every experiment. After 16-18 hours incubation, cells that did not invade were scraped off the top chamber with a cotton swab. Cells were fixed in methanol and stained with 1% Toluidine Blue or 0.2% Crystal Violet. 4 distinct fields were photographed. Data is reported as the mean and standard deviation of 3 replicates, quantified as percent that migrated through Matrigel vs. through the membrane without Matrigel.

RNA-sequencing

RNA samples were sequenced on the Illumina Hi-Seq 2000/2500 platform (one replicate; 125bp PE) and the Illumina Hi-Seq 4000 platform (two replicates; 150bp PE) (See Supplemental Experimental Procedures). We obtained approximately 60-80 million reads per library. Reads were mapped to the human genome (hg19) using TopHat2(Kim et al., 2013), and significant changes in gene expression patterns were determined using Cufflinks/Cuffdiff(Trapnell et al., 2010). Gene ontology was analyzed using GOrilla (Eden et al., 2007; Eden et al., 2009). Alternative splicing was analyzed using Vast-tools (Irimia et al., 2014). RNA abundance for genes of interest were validated using qRT-PCR, and alternative splicing events of interest were validated with PCR and 1% agarose gel (See Supplemental Experimental Procedures).

UPLC-MS/MS

Samples were analyzed using a nanoACQUITY UPLC system (Waters Corporation, Milford, MA) coupled to a Q Exactive HF Orbitrap high resolution accurate mass tandem mass spectrometer (ThermoFisher Scientific, Bremen, Germany) via a nanoelectrospray ionization source (See Supplemental Experimental Procedures). Individual proteins of interest were validated by Western blotting (See Supplemental Experimental Procedures).

ADD1 shRNA

TRC1 lentiviral plasmids targeting ADD1 or a non-target negative control were obtained from Duke University's Functional Genomics shared resource. To control for off-target effects, 3 individual shRNAs and a non-targeting shRNA were used (See Supplemental Experimental Methods).

Establishing a primary cell-derived system of tumorigenesis

293T/17 cells were co-transfected with p0467/pcl-10A (gift of Dr. Chris Counter) and individual pBabe plasmids containing transgenes of interest (Table) using FuGENE-6 (Roche, Basel, Switzerland). 24 hours later, the transfection was repeated. 8 hours after the second transfection, the media was replaced with fresh MEGM, and cells were incubated in this new media for 48 hours. Amphotropic retrovirus-containing media was harvested from the cells and filtered through a sterile 0.45µm Acrodisc with an HT tuffryn membrane (VWR, Radnor, PA). All media was snap-frozen in liquid nitrogen and stored at -80 C. Fresh MEGM was added to the 293T/17 cells, and 12 hours later media was harvested, filtered and snap frozen as done previously. Media containing the pBabe-hTERT amphotropic retroviruses was thawed at 37C. Polybrene (hexadimethrine bromide, Sigma-Aldrich, St. Louis, MO) was added to a concentration of 4µg/ml, and the media was added to primary HMECs. 12 hours later, the procedure was repeated with the second pBabe-hTERT amphotropic retrovirus containing media. This procedure was repeated every 12 hours until the HMECs were transduced with each plasmid listed in Table 1. Cells without H-Ras were saved as the immortalized (IMO) cell line. Cells that were Ras-transformed are referred to as the transformed (TFO) cell line. Cells were selected sequentially with the following antibiotics, with a 5 day recovery between drug selections: Hygromycin: 80µg/ml for 7 days; G418: 250µg/ml for 10 days; Puromycin: 0.5µg/ml for 5 days; Zeocin: 800µg/ml for 8 days; Blasticidin: 4.5µg/ml for 7 days. RAS-transformed cells were sorted by flow cytometry for YFP expression. Transgene expression was tested with qRT-PCR, UPLC/MS-MS, and anchorage-independent growth was assessed with a soft agar assay.

Transgene	Selection Marker	Source
hTERT	Hygromycin	addgene plasmid #1773, gift of Dr. Bob Weinberg (Counter et al., 1998)
$p53^{DD}$	G418	gift of Dr. Chris Counter (Hahn et al., 2002)
Cyclin D1	Puromycin	addgene plasmid #9050, gift of Dr. William Hahn
$CDK4^{R24C}$	Zeocin	gift of Dr. Chris Counter (Hahn et al., 2002)
$C\text{-}myc^{T58A}$	Blasticidin	gift of Dr. Chris Counter (Yeh et al., 2004)
$H\text{-}RAS^{G12V}$	YFP	gift of Dr. Chris Counter (Hahn et al., 1999)
Control	GFP	addgene plasmid #10668, gift of Dr. William Hahn

Table S2: Plasmids used to generate a genetically-defined system of tumorigenesis. Realated to Figure 1.

RNA-sequencing

Total RNA was obtained from cells using the TRIsure reagent (Bioline, Luckenwalde Germany) according to the manufacturer's protocol. RNA quantity was analyzed using a NanoDrop spectrophotometer, and ribosomal RNA was depleted using the Ribozero Gold kit (Epicentre, Madison, WI, USA). 50ng of rRNA depleted RNA was used as input for sequencing libraries, which were made using the ScriptSeq v2 RNA-seq library preparation kit (Epicentre) according to the manufacturer's instructions. 16 amplification cycles were used in the final PCR amplification step. Libraries were checked with a BioAnalyzer, and sequenced on the Illumina Hi-Seq 2000/2500 platform (one replicate; 125bp PE) and the Illumina Hi-Seq 4000 platform (two replicates; 150bp PE) at Duke University's Center for Genomic and Computational Biology.

Quantitative Real-time PCR

Total RNA was isolated from cells using TriSure (Bioline, Luckenwalde Germany) and reverse transcribed using the iScript cDNA synthesis kit (Bio-Rad, Hercules, CA), both according to the manufacturer's recommendations. Quantitative real-time PCR was performed using the Roche Lightcycler with Sybr green detection (Invitrogen, Carlsbad, CA). Amplification of a single product was confirmed by melting curve analysis, and the ΔΔCt analysis method was used. Data are reported as mean and standard deviation with p-values calculated using a standard t-test.

Gene	Forward Primer	Reverse Primer
GapDH	5'-CAT GTT CGT CAT GGG TGT GAA CCA-3'	5'-AGT GAT GGC ATG GAC TGT GGT CAT-3'
VIM	5'- GAC CAG CTA ACC AAC GAC AAA GC -3'	5'-CAG AGA CGC ATT GTC AAC ATC CTG -3'
CDH2	5'-GAG GAG TCA GTG AAG GAG TCA GC -3'	5'- ATC AGA CCT GAT CCT GAC AAG CTC -3'
CDCA5	5'- CTG GCC GAA GAC ACC CAG T -3'	5'- GTC CTC CTT AGT AAG CTC CCT GC -3'
RIOK1	5'- GCG GAC TCC TCT GAC AGT GAA AAC -3'	5'- TCC AGA CAT AAC CCT TGG CGA G -3'
ADD1	5'- TGG TAT GGT GAC TCC TGT GAA CG -3'	5'- GCT CGG AGT TCA CTC TGG TTG TG -3'
DBNL	5'- GGG TTG GTA AAG ACA GCT TCT GG -3'	5'- CAC ATG TTG ACC CCT GCT CAT TTC -3'
FLRT3	5'- CGT CTT CCT GGA GAT GCT CAG T -3'	5'- GGT AGC TTC CGT TAC TTC AGA ACC -3'
BLVRB	5'- ACT CCT CCA GGC TGC CAT C -3'	5'- ATC ACT GTC GTG GGA CTG AGG -3'
AKR12C	5'- GAC CCA GTC CTT TGT GCC TTG -3'	5'-GGA ATT CAA ACA CCT GCA CGT TC -3'

Table S3: Sequences for primers used to validate RNA-sequencing data. Related to Figure 2 and Figure 4.

Alternative Splicing Validation

Total RNA was isolated from cells using TriSure (Bioline, Luckenwalde Germany) and reverse transcribed using the iScript cDNA synthesis kit (Bio-Rad, Hercules, CA), both according to the manufacturer's

recommendations. PCR was performed using Taq DNA polymerase (Invitrogen, Carlsbad, CA), and PCR products were visualized on a 1% agarose gel.

Gene	Forward Primer	Reverse Primer	Description
CD44	5'- CGT GAT GGC ACC CGC TAT G -3'; Exon 5	5'- CTT CTT GAC TCC CAT GTG AGT GTC -3'; Exon 16	CD44V- Exons 1-19=1451bp product CD44E- 1-5, 12-19= 703bp product CD44S- Exons 1-5, 15-19= 307bp product
CTNND1	5'- TTC TCA GCA CCT TGG CGA AG -3'; Exon 1	5'- CTG CAT CCT GGG GAT GGT G -3'; Exon 5	Inclusion of exons 2 and 3 =664bp product
ENAH	5'- GGC CTC TTC AAC AAG TAC ACC TG -3'; Exon 10	5'- CTG CTT CAG CCT GTC ATA GTC AAG -3'; Exon 12	Exclusion of 63bp between exons 11 and 12= 169bp product
MYO1B	5'- CCA GCA GAC AAA GAG TTC CGC -3'; Exon 21	5'- AGC TCC TTG TGA GTA GAA TCC AAG -3'; Exon 26	Inclusion of exons 23 and 24= 501bp product
DLG1	5'- GGT CGG AGT GAT TCC CAG TAA AC -3'; Exon 17	5'- AGA CGT ATT CTT CTT GAC CAG GTA -3'; Exon 20-21	Mutually exclusive exon 19= 66bp size difference

Table S4: Sequences for primers used to validate alternative splicing. Related to Figure 2.

UPLC-MS/MS:

Sample Preparation: Cells were scraped in 250 µl of ammonium bicarbonate pH 8.0 (AmBic) containing 0.25% (w/v) acid labile surfactant (ALS-1). After freeze-thawing, samples were lysed by probe sonication (3 x 3 s) on ice. After centrifugation, protein concentration was determined by Bradford assay. 10µg of each sample was normalized to equal volumes with lysis buffer followed by addition of 10mM DTT. Samples were heated at 80 ºC for 10 min to denature and reduce the samples. After cooling to room temperature, samples were alkylated with 25mM iodoactamide (IAM). Excess IAM was quenched by addition of 10mM DTT. 1:25 (w/w) Sequencing Grade modified trypsin (Promega, Madison, WI) was added and samples were incubated overnight at 37ºC on a Thermomixer. After overnight digestions, ALS-1 was degraded by addition of trifluoroacetic acid (TFA) and acetonitrile (MeCN) to 1% and 2% (v/v) respectively, followed by heating at 60ºC for 2h and centrifuging to remove degraded ALS-1. Finally, 50 fmol/µl of trypsinized yeast ADH1 (Massprep; Waters Corporation, Milford, MA) was added and samples were transferred to Maximum Recovery LC vials (Waters).

Quantitative Proteomic Analysis: Quantitative one-dimensional LC-MS/MS was performed once per sample using 500ng of peptide digest. Samples were analyzed using a nanoACQUITY UPLC system (Waters) coupled to a Q Exactive HF Orbitrap high resolution accurate mass tandem mass spectrometer (Thermo) via a nanoelectrospray ionization source at Duke University's Proteomics and Metabolomics Core Facility. Briefly, the sample was first trapped on a Symmetry C18 300 µm x 20 mm trapping column (5 µl/min at 99.9/0.1 v/v H2O/MeCN for 5 min), after which the analytical separation was performed using a 1.7 µm ACQUITY HSS T3 C18 75 µm x 250 mm column (Waters) using a 90 min gradient of 5 to 30% MeCN with 0.1% formic acid at a flow rate of 400 nl/min with a column temperature of 55ºC. Data collection on the Q Exactive HF mass spectrometer was performed in a data-dependent MS/MS manner, using a 120,000 resolution precursor ion (MS1) scan followed by MS/MS (MS2) of the top 12 most abundant ions at 30,000 resolution. MS1 was accomplished using an automatic gain control (AGC) target of 3e6 ions and 50 msec maximum injection time. MS2 used AGC target of 5e4 ions and 45 ms maximum injection time, 1.2 m/z isolation window, 27 V normalized collision energy, and 20 s dynamic exclusion. The total analysis cycle time for each sample injection was approximately 2 h. Samples included two QC pool samples for column condition and additional QC pool samples analyzed at the beginning, middle and end of the study. Following the analyses, the data was imported into Rosetta Elucidator v4.0 (Rosetta Biosoftware, Inc.), and all LC-

MS files were aligned based on the accurate mass and retention time of detection ion ("features") using a PeakTeller algorithm (Elucidator). The relative peptide abundance was calculated based on area-under-the-curve (AUC) of aligned features across all runs. The dataset had 368,613 quantified features and HCD fragmentation was performed to generate approximately 892,447 MS/MS spectra for sequencing by database searching. This MS/MS data was searched against the reviewed (Swiss-Prot) protein sequences in the Uniprot (www.uniprot.org) database with Homo Sapiens taxonomy (downloaded on 08/16/16) as well as the study-specific proteins mouse p53DD, human R24C CDK4, T58C c-Myc and G12V H-ras, as well as the contaminant bovine serum albumin and surrogate standard yeast ADH1. In addition, the database contained an equal number of and reverse "decoy" protein sequences for false discovery rate determination (and a total of 40,407 entries). Amino acid modifications allowed in database searching included fixed carbamidomethyl on Cys, and variable deamidation of Asn/Gln, peptide N-terminal Gln->pyroGlu and protein N-terminal acetylation; variable modifications were deemed appropriate for these samples by a preliminary analysis using Byonic Preview (Protein Metrics, Inc). The data was searched with 7 ppm precursor, 0.02 Da product ion tolerance, and tryptic enzyme specificity, allowing up Project 1089: cancer vs normal HMECs to two missed cleavages. The data was annotated at 0.4% peptide FDR using the PeptideTeller algorithm in Rosetta Elucidator.

Western blots

Whole cell lysates were prepared by scraping into cold 0.1% SDS lysis buffer. Protein was cleared by centrifugation, quantified with a Bradford assay, and boiled in Laemmli loading buffer. ~20µg of protein was then size separated on a criterion SDS PAGE gel (Biorad, Hercules, CA, USA). Protein was transferred onto nitrocellulose membrane, and transfer was verified using Ponceau S staining. Membranes were blocked with 5% Non-fat milk in TBS+0.1% Tween20 (TBST) for one hour at room temperature, incubated with primary antibody at 4C overnight, washed thoroughly with TBST, incubated with secondary antibody for one hour at room temperature, washed extensively with TBST, and then developed using SuperSignal West Pico Chemiluminescent Substrate (ThermoFisher Scientific), and exposed to film. All primary antibodies are listed below. Anti-mouse (515-035-062) and anti-rabbit (111-035-003) HRP conjugated secondary were purchased from Jackson ImmunoResearch (West Grove, PA, USA) and used at a 1:20000 dilution.

Gene	Antibody Source and catalog number	Dilution
GapDH	Santa Cruz; sc-47724	1:1000
B-tubulin	Santa Cruz; sc-5274	1:1000
VIM	Santa Cruz; sc-6260	1:250
CDH2	Santa Cruz; sc-271386	1:250
CDCA5	Santa Cruz; sc-365319	1:200
RIOK1	Proteintech; 17222-1-AP	1:500
ADD1	Santa Cruz; sc-33633	1:200
DBNL	Santa Cruz; sc-398498	1:200
FLRT3	Santa Cruz; sc-514482	1:200
BLVRB	Santa Cruz; sc-373692	1:200
AKR1C2	Iowa Hybridoma Bank	0.375µg/ml

Table S5: Primary antibodies used for validation Western blots. Related to Figure 4.

ADD1 shRNA knockdown:

HEK-293T cells were grown to ~70% confluency and co-transfected with 1µg shRNA lentiviral plasmid (see table), 900ng psPAX2 packaging plasmid (a gift from Didier Trono; Addgene plasmid #12260), and 100ng pMD2.G envelope plasmid (a gift from Didier Trono; Addgene plasmid #12259) using FuGENE-6 transfection reagent (Promega, Madison, WI). Media was changed to DMEM+30%FBS 16 hours post-transfection. Virus-containing supernatant was harvested 48 and 72 hours post-transfection and filtered with a 45µM filter.

Hexadimethrine bromide (Sigma-Aldrich, St. Louis, MO) was added to 8µg/ml final concentration, and 0.5ml of prepared viral supernatant was added to IMO cells and incubated for 48 hours. ADD1 knockdown was assessed with a western blot.

TRC_ID (plate map)	Olig_Seq	Gene	Refseq
	CCGGGCGCGATAGCGCTAATAATTTCTCGAGAAATTATTAGCGCTATCGCGCTTTTTG	Neg ctrl shRNA	Non-targeting sequence
84018	CCGGGCAGGTTTACAATTTAGCTTACTCGAGTAAGCTAAATTGTAAACCTGCTTTTTG	ADD1 (shRNA 1)	NM_001119.3,NM_014189.2, NM_014190.2,NM_176801.1
84019	CGGCGGTGTAAATTGGCAGCGTTTCTCGAGAAACGCTGCCAATTTACACCGTTTTTG	ADD1 (shRNA 2)	NM_001119.3,NM_014189.2,NM_014190.2,NM_176801.1
84020	CCGGGCAGGAATTTGAAGCCCTCATCTCGAGATGAGGGCTTCAAATTCCTGCTTTTTG	ADD1 (shRNA 3)	NM_001119.3,NM_014189.2,NM_014190.2,NM_176801.1

Table S6: TRC1 lentiviral shRNA clones. Related to Figure 4.

Data and Software Availability

All data has been deposited in GEO and can be accessed by GEO series accession number GSE110677.

Supplemental References:

Bisogno, L.S., and Keene, J.D. (2017). Analysis of post-transcriptional regulation during cancer progression using a donor-derived isogenic model of tumorigenesis. Methods *126*, 193-200.

Counter, C.M., Hahn, W.C., Wei, W., Caddle, S.D., Beijersbergen, R.L., Lansdorp, P.M., Sedivy, J.M., and Weinberg, R.A. (1998). Dissociation among in vitro telomerase activity, telomere maintenance, and cellular immortalization. Proc Natl Acad Sci U S A *95*, 14723-14728.

Eden, E., Lipson, D., Yogev, S., and Yakhini, Z. (2007). Discovering motifs in ranked lists of DNA sequences. PLoS Comput Biol *3*, e39.

Eden, E., Navon, R., Steinfeld, I., Lipson, D., and Yakhini, Z. (2009). GOrilla: a tool for discovery and visualization of enriched GO terms in ranked gene lists. BMC Bioinformatics *10*, 48.

Hahn, W.C., Dessain, S.K., Brooks, M.W., King, J.E., Elenbaas, B., Sabatini, D.M., DeCaprio, J.A., and Weinberg, R.A. (2002). Enumeration of the simian virus 40 early region elements necessary for human cell transformation. Mol Cell Biol *22*, 2111-2123.

Irimia, M., Weatheritt, R.J., Ellis, J.D., Parikshak, N.N., Gonatopoulos-Pournatzis, T., Babor, M., Quesnel-Vallieres, M., Tapial, J., Raj, B., O'Hanlon, D*., et al.* (2014). A highly conserved program of neuronal microexons is misregulated in autistic brains. Cell *159*, 1511-1523.

Kim, D., Pertea, G., Trapnell, C., Pimentel, H., Kelley, R., and Salzberg, S.L. (2013). TopHat2: accurate alignment of transcriptomes in the presence of insertions, deletions and gene fusions. Genome Biol *14*, R36.

Trapnell, C., Williams, B.A., Pertea, G., Mortazavi, A., Kwan, G., van Baren, M.J., Salzberg, S.L., Wold, B.J., and Pachter, L. (2010). Transcript assembly and quantification by RNA-Seq reveals unannotated transcripts and isoform switching during cell differentiation. Nat Biotechnol *28*, 511-515.

Yeh, E., Cunningham, M., Arnold, H., Chasse, D., Monteith, T., Ivaldi, G., Hahn, W.C., Stukenberg, P.T., Shenolikar, S., Uchida, T*., et al.* (2004). A signalling pathway controlling c-Myc degradation that impacts oncogenic transformation of human cells. Nat Cell Biol *6*, 308-318.